ON THE SHOULDERS OF GIANTS: PROPERTIES OF THE STELLAR HALO
AND THE MILKY WAY MASS DISTRIBUTION

PRAJWAL RAJ KAFLE[1,2], SANJIB SHARMA[1], GERAINT F. LEWIS[1], AND JOSS BLAND-HAWTHORN[1]

[1] Sydney Institute for Astronomy, School of Physics A28, The University of Sydney, NSW 2006, Australia; p.kafle@physics.usyd.edu.au
[2] International Centre for Radio Astronomy Research (ICRAR), The University of Western Australia, 35 Stirling Highway, Crawley, WA 6009, Australia

ABSTRACT

Halo stars orbit within the potential of the Milky Way, and hence their kinematics can be used to understand the underlying mass distribution. However, the inferred mass distribution depends sensitively on assumptions made on the density and the velocity anisotropy profiles of the tracer population. Also, there is a degeneracy between the parameters of the halo and those of the disk or bulge. Most previous attempts that use halo stars have made arbitrary assumptions about these. In this paper, we decompose the Galaxy into three major components—a bulge, a Miyamoto–Nagai disk, and a Navarro–Frenk–White dark matter halo – and then model the kinematic data of the halo blue horizontal branch and K-giant stars from the Sloan Extension for Galactic Understanding and Exploration. Additionally, we use the gas terminal velocity curve and the Sgr A* proper motion. With the distance of the Sun from the center of the Galaxy $R_\odot = 8.5$ kpc, our kinematic analysis reveals that the density of the stellar halo has a break at $17.2^{+1.1}_{-1.0}$ kpc and an exponential cutoff in the outer parts starting at $97.7^{+15.6}_{-15.8}$ kpc. Also, we find that the tracer velocity anisotropy is radially biased with $\beta_s = 0.4 \pm 0.2$ in the outer halo. We measure halo virial mass $M_{\rm vir}$ to be $0.80^{+0.31}_{-0.16} \times 10^{12}\ M_\odot$, concentration c to be $21.1^{+14.8}_{-8.3}$, disk mass to be $0.95^{+0.24}_{-0.30} \times 10^{11}\ M_\odot$, disk scale length to be $4.9^{+0.4}_{-0.4}$ kpc, and bulge mass to be $0.91^{+0.31}_{-0.38} \times 10^{10}\ M_\odot$. The halo mass is found to be small, and this has important consequences. The giant stars reveal that the outermost halo stars have low velocity dispersion, but interestingly this suggests a truncation of the stellar halo density rather than a small overall mass of the Galaxy. Our estimates of local escape velocity $v_{\rm esc} = 550.9^{+32.4}_{-22.1}$ km s^{-1} and dark matter density $\rho^{\rm DM}_\odot = 0.0088^{+0.0024}_{-0.0018}\ M_\odot$ pc^{-3} $(0.35^{+0.08}_{-0.07}$ GeV cm$^{-3})$ are in good agreement with recent estimates. Some of the above estimates, in particular $M_{\rm vir}$, are dependent on the adopted value of $R_\odot$ and also on the choice of the outer power-law index of the tracer number density.

Key words: dark matter – Galaxy: fundamental parameters – Galaxy: halo – Galaxy: kinematics and dynamics – stars: horizontal-branch

Online-only material: color figures

1. INTRODUCTION

Mass is the fundamental property of any galaxy. An accurate measurement of the Galaxy mass has repercussions in many sectors, e.g., in its mass assembly history (Wechsler et al. 2002), identifying a realistic Galaxy in a simulation (e.g., Vera-Ciro et al. 2013; Wang et al. 2012), or its analogue (Robotham et al. 2012), simulating the tidal streams or the orbit of the satellite galaxies (e.g., Newberg et al. 2010), studying the tidal impact of the Galaxy on the satellite galaxies (e.g., Johnston 1998; Kallivayalil et al. 2013; Nichols et al. 2014), etc. Various approaches have been undertaken to determine the mass distribution of the Galaxy, e.g., the timing argument (Kahn & Woltjer 1959; Li & White 2008), the local escape speed (Leonard & Tremaine 1990; Smith et al. 2007; Piffl et al. 2014), the orbital evolution of the satellite galaxies and globular clusters (Lin & Lynden-Bell 1982; Boylan-Kolchin et al. 2013), modeling the tidal streams (Law et al. 2005; Newberg et al. 2010; Sanders & Binney 2013b; Sanderson & Helmi 2013), the H I gas rotation curve (e.g., Sofue et al. 2009), fitting a parameterized model to the available observational constraints (e.g., Dehnen & Binney 1998; McMillan 2011; Irrgang et al. 2013), etc. Each of these methods has its own inherent limitation, for example, the local escape speed method suffers from the paucity of high-velocity stars, and also it is unclear whether the phase space

is fully filled up to the escape velocity. The use of an H I gas rotation curve suffers from the fact that there is no extended H I disk reported for the Galaxy, and hence it fails to probe the mass that lies beyond the extent of the disk. For an in-depth discussion and description of the various methods, we refer the reader to two recent reviews by Courteau et al. (2014) on the Galaxy masses and by Sofue (2013) and references therein on the rotation curve.

A simple yet robust method to probe the Galaxy mass is provided by an application of the Jeans (1915) equation. The spherical Jeans equation for a system in dynamic equilibrium is given by

$$-\rho \frac{d\Phi}{dr} = \frac{d\rho\sigma_r^2}{dr} + \rho\sigma_r^2 \frac{2\beta}{r}, \tag{1}$$

where Φ is gravitational potential, ρ is stellar density, σ_r is radial velocity dispersion, and β is velocity anisotropy, and all of them can be a function of galactocentric distance r. Thanks to massive stellar surveys such as Sloan Digital Sky Survey (SDSS)/Sloan Extension for Galactic Understanding and Exploration (SEGUE) that provide a catalog of position and radial velocity measurements of a large number of halo tracers, it is now possible to use the Jeans analysis to put the most stringent constraints on the halo parameters out to the maximum observed distance. Among all the parameters that enter the Jeans analysis, the most uncertain quantity is velocity

anisotropy β, which is defined as

$$\beta = 1 - \frac{\sigma_\theta^2 + \sigma_\phi^2}{2\sigma_r^2}, \qquad (2)$$

where σ_θ and σ_ϕ are the velocity dispersions along the spherical polar (θ) and azimuthal (ϕ) directions, respectively. With $\beta \in [-\infty, 1]$, $\beta > 0$ signifies dominance of radial motion of stars, $\beta < 0$ signifies dominance of tangential motion, and $\beta = 0$ signifies an isotropic system. If β is not known, then the Jeans analysis suffers from a degeneracy known as *the mass-anisotropy degeneracy*. In general terms it means that the same radial velocity dispersion profile can be obtained either by lowering the β value or by increasing the mass. Numerous studies based on the kinematics of different stellar species, namely, the subdwarfs (Smith et al. 2009a), the main-sequence stars (Brown et al. 2010), and the blue horizontal branch (BHB) stars (Kafle et al. 2012, hereafter K12), concur that $\beta \sim 0.6$ (radial) in the solar neighborhood. There have been recent attempts to constrain the β beyond the solar neighborhood, including K12, who use the line-of-sight velocity of a BHB sample to measure $\beta(r)$ to a radius of $\sim$25 kpc. They find a non-monotonic trend in β starting with 0.5 (radial) at small r, which falls to -1.2 (tangential) at $r = 17$ kpc and then rises again to 0 at $\sim$25 kpc. An additional measurement of $\beta = 0.0^{+0.20}_{-0.41}$ at $r = 24$ kpc is also reported by Deason et al. (2013) in their proper-motion studies of the main-sequence halo stars obtained from the *Hubble Space Telescope* (*HST*). This measurement of β has broken *the mass-anisotropy degeneracy* at least out to $r = 24$ kpc (K12). To address the problem, practices such as reporting the masses for some arbitrary set of β (e.g., Battaglia et al. 2005) or assuming them from simulations (Xue et al. 2008) are a reasonable start. However, to avoid a bias, an approach of marginalizing over all possible values of β must be taken. It is worth noting that an independent approach for a mass modeling using halo stars and assuming the Jeans equation is only a good starting point and helpful to make a testable prediction.

One preferred approach (Battaglia et al. 2005; Xue et al. 2008; Kafle et al. 2012) with the Jeans analysis is to decompose the Galaxy into its dominant components (disk, bulge, and halo). Inherent degeneracies among the components are a major concern of this approach, and it means that assuming a higher disk and/or bulge mass would lower the halo mass and vice versa. To break the degeneracies, the entire parameter space should be explored. An alternative approach is the tracer mass formalism (Bahcall & Tremaine 1981; Watkins et al. 2010), which is based on moments. It is a robust technique to estimate the underlying mass of the system provided that the density and mass profiles are power laws and the anisotropy is constant with radius, which is certainly not true for the Galaxy.

In this paper, we work toward constructing a holistic model of the Galaxy by combining the best available data in hand, such as the proper motion of Sgr A*, the gas terminal velocity in the inner $r < R_\odot$ of the Galaxy, and kinematics of the large number of halo tracers provided by SDSS/SEGUE. Our aim is to provide the stellar halo number density and kinematic profiles out to the maximum observed distance, the dark matter halo mass and concentration, and the disk and bulge mass parameters. For this we take an approach of fitting parameterized mass models of the Milky Way to observational constraints. This is largely similar to earlier works by, e.g., Dehnen & Binney (1998), McMillan (2011), Irrgang et al. (2013), but includes detailed modeling of distant halo stars. Such a model must reproduce

known local standard estimates such as the escape velocity $v_{\rm esc} \approx 545$ km s^{-1} (Smith et al. 2007; Piffl et al. 2014), the dark matter density $\rho_\odot^{\rm DM} \approx 0.4$ GeV cm^{-3} (Catena & Ullio 2010; McMillan 2011), the total column density $\Sigma_\odot^{\rm total} \approx 70\ M_\odot$ pc^{-2} (Kuijken & Gilmore 1989a, 1989b, 1989c, 1991; Bovy & Rix 2013; Zhang et al. 2013), and the angular velocity of the Sun with respect to Galactic center $\omega_\odot \approx 30$ km s^{-1} kpc^{-1} (Reid & Brunthaler 2004; McMillan & Binney 2010).

We organized the paper as follows: in Section 2 we discuss the giant star data, outline the selection criteria (for diagnostic, see Appendix A), and estimate the distance (for full calculation, see Appendix B). In Section 3 we present the halo kinematical profile. In Section 4 we discuss the models for density, anisotropy, and potential that are used to fit the kinematics of the halo. In Section 5 we present our results and discussion. Finally, we summarize in Section 6.

2. DATA: GIANT STARS

Among the wide varieties of known halo tracers, here we are interested in K giants. These have long been studied (e.g., Ratnatunga et al. 1989; Ratnatunga & Freeman 1989; Morrison et al. 1990, etc) to probe the distant halo. K giants are brighter and hence effectively go deeper. Additionally, they are abundant in number in SEGUE (Yanny et al. 2009), a spectroscopic subsurvey of SDSS. They can therefore supplement the existing catalogs of distant tracers such as the BHB stars (Yanny et al. 2000; Sirko et al. 2004; Xue et al. 2008) and the variable stars (Watkins et al. 2009; Sesar et al. 2011).

2.1. Selection Criteria

We mine the ninth SDSS data release DR9 (Ahn et al. 2012) to construct our giant star catalog. The first set of selection criteria we impose to prepare the catalog are

$$\begin{cases} \text{Giants classified by SSPP} \\ 0.5 < m_g - m_r < 1.3, \\ 0.5 < m_u - m_g < 3.5, \\ 14 < m_r < 20, \\ \log g < 2.9, \\ \text{reddening estimate } E(B - V) < 0.25 \text{ and} \\ m_g - m_r > 0.086[{\rm Fe/H}]^2 + 0.38[{\rm Fe/H}] + 0.96, \end{cases} \qquad (3)$$

where m_g and m_r are the extinction-corrected magnitudes. The metallicity [Fe/H] and the stellar parameters we use, i.e., surface-gravity $\log g$ and effective temperature $T_{\rm eff}$, are the ones labeled in the SDSS DR9 as "ADOP," meaning the average of various estimators that the SSPP[3] pipeline uses, and also are the ones recommended by Yanny et al. (2000). The quadratic color-metallicity cut in Equation (3), devised by Xue et al. (2014) and inferred from An et al. (2008), is basically meant to eliminate the contamination from red horizontal branch and red clump stars. Note that we take a slightly conservative cut on $\log g$ to minimize the contamination of dwarfs. Additionally, we apply a second set of selection criteria given by

$$\begin{cases} \text{signal-to-noise ratio S/N} > 15 \text{ and} \\ \text{no critical and cautionary flags raised by SSPP} \end{cases} \qquad (4)$$

---

[3] SEGUE Stellar Parameter Pipeline is a pipeline that processes the spectra SEGUE obtains.

as a quality control cut. This is to ensure the accuracy and the reliability of the stellar parameters and radial velocity values that SSPP provides. Combination of the above given sets of selection criteria yields 5330 candidate giants. For further diagnostics about selection criteria and candidate giants, see Appendix A.

As shown in the next section, we estimate the most probable distance of the stars, which gives the height, z, of the stars from the Galactic plane. We then impose the condition $|z| > 4$ kpc to select the halo stars. This leaves us with 5140 stars.

2.2. Distance Estimation

Correct distance measurements of the giant stars are critical for studying the kinematics of the halo and also for modeling the mass. For a correct treatment of the observational errors, we set up the distance estimation in a Bayesian framework; the calculations are given in full in Appendix B. The procedure we follow is the same as given by Xue et al. (2014). The essence of the exercise is that for each star with some set of observables, say, $S = \{m, c, [Fe/H]\}$, we obtain a corresponding absolute magnitude by matching it to color-metallicity fiducials of red giant sequences of clusters. In the end, with the inferred absolute magnitude and a given apparent magnitude, we use the standard photometric parallax relation to compute the distance for a star. Instead of a single valued number, the setup allows us to compute a full probability distribution or posterior distribution $p(\mu|S)$ of the distance modulus μ.

3. THE VELOCITY DISPERSION PROFILE

With the distance modulus posterior distributions $p(\mu|S)$ and the line-of-sight velocities, we now proceed to determine kinematic profiles of the stellar halo, namely, the radial $\sigma_r(r)$, polar $\sigma_\theta(r)$, and azimuthal $\sigma_\phi(r)$ velocity dispersion profiles. The line-of-sight velocities we analyze are the ones provided by SSPP under the heading "ELODIERVFINAL." We find that 89% of our sample has uncertainties in radial velocity of <10 km s^{-1}. These velocities are in the heliocentric frame of reference, and for the purpose of modeling we need to transform them into the one centered at the Galactic center. For this we assume the velocity of the local standard of rest to be an IAU-adopted value of $v_{LSR} = 220$ km s^{-1}; the motion of the Sun with respect to the local standard of rest to be $U_\odot = +11.1$ km s^{-1}, $V_\odot = +12.24$ km s^{-1}, $W_\odot = +7.25$ km s^{-1} (Schönrich et al. 2010); and the distance of the Sun from the center of the Galaxy to be $R_\odot = 8.5$ kpc.

Had the full-space motion of the stars been known, one could measure $\sigma_r(r)$, $\sigma_\theta(r)$, and $\sigma_\phi(r)$ by simply dividing the sample into the radial shells and then computing the second moment of the components of the velocity. Unfortunately, we only know the velocity along one direction, i.e., along the line of sight; therefore, obtaining all three dispersion profiles requires a more careful modeling of the halo kinematics.

Given that we are only interested in the dispersion profiles, we consider a gaussian velocity ellipsoid model with rotation about the z-axis. This model does not require any a priori knowledge of the underlying potential or the tracer density distribution. Generally, the velocity ellipsoid can have a tilt, although it is evident from the recent studies by Smith et al. (2009b) and Bond et al. (2010) that the tilt with respect to the spherical coordinate system for the Galactic halo is consistent with zero, so we ignore it. Therefore, we write the velocity distribution as a function of

radius as

$$p(\mathbf{v}|\Theta, l, b, r) = \mathcal{N}(v_r|0, \sigma_r(r))\mathcal{N}(v_\theta|0, \sigma_\theta(r))$$
$$\times \mathcal{N}(v_\phi|v_{rot}, \sigma_\phi(r)), \quad (5)$$

where the model $\Theta = \{\sigma_r, \sigma_\phi, \sigma_\theta, v_{rot}\}$ is given by

$$\sigma_r(r) = \text{Interpolation}(\sigma_{r,m}, r_m)$$
$$\sigma_\theta(r) = \text{Interpolation}(\sigma_{\theta,m}, r_m)$$
$$\sigma_\phi(r) = \text{Interpolation}(\sigma_{\phi,m}, r_m), \text{ and}$$

the notation $\mathcal{N}$ represents the gaussian distribution centered at $\bar{x}$ and with dispersion σ given by

$$\mathcal{N}(x|\bar{x}, \sigma) = \frac{1}{\sqrt{2\pi}\sigma}\exp\left[-\frac{(x-\bar{x})^2}{2\sigma^2}\right]. \quad (6)$$

Here r_m are grid points in radius r, which we call nodes. Each of these nodes will have a corresponding value of the velocity dispersion. Thus, the final dispersion profile is obtained from a linear interpolation over the nodes.

While the location of the nodes can be fixed arbitrarily, for a more systematic approach, we choose them such that for $r < 70$ kpc each node has 500 stars. For $r > 70$ kpc, as a result of fewer stars, we choose them such that each node has 30 stars. This is a nonparametric approach to obtaining a kinematic profile and is a useful technique in our case for two reasons. First, we do not have an exact distance but a probability distribution of distance modulus $p(\mu)$ of each star in our sample. Hence, unlike previous studies, e.g., Kafle et al. (2012, 2013), the data cannot be segregated into the radial bins because a star near a bin edge could have some finite probability to be in a neighboring bin. In fact, depending on the distance probability of each star, this approach enables each star to make an appropriate contribution to each node where $p(\mu)$ is nonzero. Second, in Kafle et al. (2012) undulations were reported in the kinematic profiles of the BHB stars. Hence, we do not want to restrict our analysis by making an assumption about the functional forms of σ_r, σ_θ, and σ_ϕ.

In the absence of proper-motion information, we marginalize Equation (5) over the tangential velocities, v_l and v_b. The resultant marginalized distribution function (DF) can be expressed as

$$p(v_{los}|\Theta, l, b) \propto \iiint p(\mathbf{v}|\Theta, l, b, \mu)p(\mu)\, dv_l\, dv_b\, d\mu. \quad (7)$$

Above the DF is convolved with the distance modulus posterior of each star $p(\mu)$ from Equation (B1). The convolution corrects for the spatial selection effect and also enables us to propagate the distance uncertainties to our final estimate of the kinematic profiles.

Finally, to obtain the dispersion profiles, we use the likelihood estimation technique based on Markov Chain Monte Carlo (MCMC) random walks. For all experiments below, we use an MCMC algorithm, namely, a stretch move as described in Goodman & Weare (2010) to sample from the posterior probability distribution given by our model. Our MCMC walks were run for sufficient autocorrelation time, so as to ensure that the distributions of parameters were stabilized around certain values. The advantage of this method over standard MCMC algorithms such as Metropolis–Hastings is that this method explores the parameter space efficiently and also produces independent samples with a much shorter autocorrelation time.
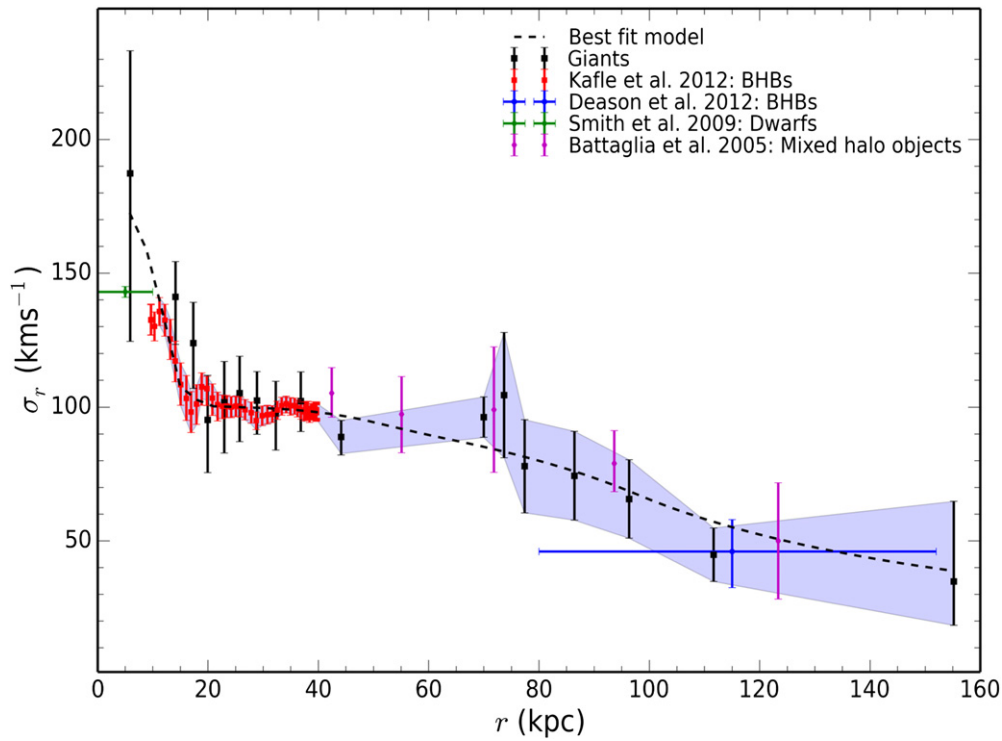
Figure 1. Radial velocity dispersion profile, $\sigma_r(r)$, of the stellar halo. The black squares with error bars are the σ_r values for the giants computed in this paper, the red squares with error bars are the estimates for BHB stars taken from K12, the blue dot with error bar is the measured value for BHB stars from Deason et al. (2012), the magenta dots with error bars are Battaglia et al. (2005) combined estimate for the mixed sample of halo objects populating at large r, and the green dots with horizontal and vertical error bars are the reported values for SEGUE subdwarfs by Smith et al. (2009a). The dashed black line is our best-fit model for a combined BHB and giant sample (the shaded purple region).

(A color version of this figure is available in the online journal.)

The log-likelihood function, $\mathcal{L}$, we use is

$$\mathcal{L}(\Theta) = \sum_{i=1}^{n} \log p(v_{\text{los},i}|\Theta, l_i, b_i), \qquad (8)$$

where the sum is over the total number of stars n. The MCMC run gives us the posterior distributions of the model parameters $\Theta = \sigma_r, \sigma_\theta, \sigma_\phi, v_{\text{rot}}$ at given distances. The values corresponding to the highest likelihood are considered the best estimates of the model parameters, and the uncertainties are computed from the 16th and 84th percentile of the distributions.

Our σ_r profile of the halo giants is shown in Figure 1 by black squares. It starts high at 190 km s^{-1}, in the inner region, drops to 100 km s^{-1} at distance $r \sim 20$ kpc, and then remains flat till $r \sim 70$ kpc. This is consistent with the trend seen in BHB stars (Kafle et al. 2012), shown by red squares. However, note that the break in the $\sigma_r(r)$ profile of BHB stars is at a radius of $\sim$17 pc, which is slightly smaller than that of the giants. We suspect this to be due to larger distance errors of giants. Distance errors will have the effect of smoothing sharp transitions. At radius $r > 70$ kpc, for giants we find that there is a further drop in the σ_r, reaching as low as 35 km s^{-1} at $\sim$155 kpc. The magenta data point taken from Battaglia et al. (2005) also shows a low σ_r at such a large distance. Similarly, in the range $r \sim 100$–150 kpc Deason et al. (2012) find a low $\sigma_r \approx 50$–60 km s^{-1} among their BHB sample (blue data). Similar trends in $\sigma_r(r)$ for different populations reported above are reassuring, since they trace the same gravitational potential. The large error bar in the $\sigma_r(r)$ value for the giant sample at $r \sim 5.9$ kpc is because, close to the Sun and along the Galactic pole, the contribution of the radial velocity to the line-of-sight velocity is low.
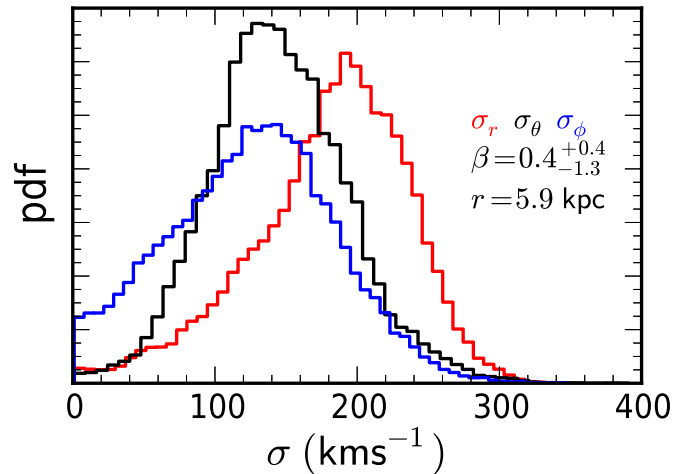

Figure 2. Posterior distributions of the velocity dispersions of the giants at $r = 5.9$ kpc; the red, black, and blue lines show the probability distribution functions for σ_r, σ_θ, and σ_ϕ, respectively.

(A color version of this figure is available in the online journal.)

Although we can measure σ_r, we are unable to constrain the tangential components of the dispersion, σ_θ and σ_ϕ, for the following reasons. First, with a line-of-sight component of the velocity alone, we cannot measure the tangential dispersions at distances $r \gg R_\odot$. Second, the distance uncertainty of our sample of giants is large, rendering large uncertainties in the tangential dispersions. However, at the first node $r \sim 5.9$ kpc the tangential velocity contributes significantly to v_{los}, which makes it possible to compute σ_θ and σ_ϕ; see Figure 2. Here we find

that the halo is radial, $\beta = 0.4^{+0.4}_{-1.3}$, which is in agreement with the previous results using the subdwarfs (Smith et al. 2009a), the main-sequence stars (Bond et al. 2010), and the BHB stars (Kafle et al. 2012) at a similar distance.

The issue we ignore in this study is the effect of substructures on kinematics. In K12, it was shown that the effect of the two most dominant structures in the halo, the Sagittarius stellar stream and the Virgo overdensity, is negligible.

4. FITTING THE MODEL

We now proceed to modeling the $\sigma_r(r)$ profile of the halo in order to probe the Galactic potential, $\Phi(r)$. For this we rearrange the Jeans Equation (1) as

$$\frac{d\sigma_r(r)^2}{dr} = -\frac{1}{r}\left[r\frac{d\Phi(r)}{dr} + \sigma_r(r)^2\left(2\beta(r) + \frac{d\ln\rho(r)}{d\ln r}\right)\right]. \quad (9)$$

We solve this first-order differential equation in r numerically, forcing a boundary condition $r \to \infty$ as $\sigma_r \to 0$. For some supplied profile for potential Φ, density ρ, and anisotropy β, we use the numerical solution for $\sigma_r(r)$ to fit the observed $\sigma_r(r)$ obtained in Section 3 (Figure 1). In the following sections we describe parametric forms of $\Phi(r)$, $\rho(r)$, and $\beta(r)$ that are used in our model; for a quick reference see Table 1.

4.1. Density $\rho(r)$

Studies of the morphology of the Milky Way halo suggest that a good fit to the stellar halo density distribution is a double power law with a shallow slope inside a break radius (r_b) and a sharp fall-off outside. For example, analyzing the main-sequence turnoff stars, Bell et al. (2008) conclude that a power law, $\rho \propto r^{-\alpha}$, with index of $\alpha = 2$ for the inner region and 4 in the outer region with a break at $r \lesssim 20$ kpc is a reasonable representation. Similar conclusions were also made by Watkins et al. (2009) in their studies of RR Lyrae stars out to 100 kpc and by Deason et al. (2011) for BHB stars out to 40 kpc. Apart from SDSS, the study by Sesar et al. (2011) of the main-sequence turnoff stars obtained from the Canada–France–Hawaii Telescope Legacy Survey suggests a slightly shallower fall of 3.8 beyond the break radius $r = 28$ kpc. More recently, Sesar et al. (2013) using variable stars suggest a broken power law but with a much smaller break radius of ~ 16 kpc. In agreement with Watkins et al. (2009), Deason et al. (2011), here we adopt a double power-law fit to the halo density with an inner slope of 2.4 and an outer slope of 4.5 with break at radius r_b. As we will discuss later, the drop seen in the σ_r profile at $r \approx 20$ kpc seems likely to be a consequence of the break in the density. Hence, to further investigate this issue, we keep the break radius (r_b) as a free parameter of our model.

The outermost ($r \gtrsim 100$ kpc) region of the halo is diffuse and highly structured (Sesar et al. 2007; Sharma et al. 2011b). Only a handful of stars have been observed at such large distances, and so the density profile is largely unknown. With a catalog of a comparatively larger number of outermost halo stars, we investigate what the decline of $\sigma_r(r)$ after $r \gtrsim 90$ kpc tells us about the density profile. For this, we investigate a truncated model of the outer halo with a truncation radius r_t. A similar approximation has also been made by Dehnen et al. (2006), but with a forced sharp truncation at $r = 160$ kpc. However, we soften the truncation by using an exponential functional form that has a tunable parameter Δ that determines the strength of the fall (see also Sharma et al. 2012). We then let the MCMC

likelihood fit determine both the position of r_t and the scale length of the fall Δ. The first row in Table 1 shows the form of the density profile that we adopt. Note that we assume the logarithmic slope at $r = r_t$ to be continuous. This gives $\epsilon = (r_t/\Delta) - 4.5$, and the slope at $r \geqslant r_t$ as $\epsilon - r/\Delta$.

4.2. Anisotropy $\beta(r)$

The velocity anisotropy (β) is the most uncertain quantity that enters the Jeans equation, and only recently has $\beta(r)$ been measured directly. The full phase-space studies of the subdwarfs in Smith et al. (2009a) and main-sequence stars in Brown et al. (2010) suggest that the halo within $d < 10$ kpc is radial with $\beta \approx 0.7$. Recently, K12 studied the line-of-sight velocity of BHB stars and found that at a similar distance range ($r < 12$ kpc) the halo is radial $\beta \sim 0.5$. Moreover, K12 also found that the $\beta(r)$ profile of the stellar halo has features that include a tangential dip ($\beta = -1.2$) at $r \sim 17$ kpc. In the range $19 \lesssim r/\text{kpc} \lesssim 25$, K12 find the β to be consistent with zero given the uncertainty. Further confirmation of this comes from Deason et al. (2013), who used the *HST* proper-motion information of the main-sequence stars to find that at similar distance $r \sim 25$ kpc the halo is isotropic $\beta = 0.0^{+0.4}_{-0.2}$. For $r > 25$ kpc, so far there has been no direct measurement of $\beta(r)$. Therefore, in this regime we have no choice but to assume some model for β. A trend that $\beta(r)$ rises from 0 and attains a positive value at large distances has been reported (see Figure 13 of K12) for the ΛCDM stellar halos of Bullock & Johnston (2005) and also for the halo stars in the cosmological simulations of Sales et al. (2007). We assume a similar trend here, i.e., at distance $r > r_2$, $\beta(r)$ is constant and equal to the β_s value. However, in between the maximum observed radius $r = 25$ kpc and the distance r_2, $\beta(r)$ is assumed to be linear. This is more physical than introducing an abrupt transition like a step function. In other words, r_2 determines the slope of the $\beta(r)$ profile joining β_s and $\beta|_{r=25\,\text{kpc}}$. Here we assume r_2 to be 50 kpc. This transition is also consistent with the results from the simulation. However, in both of the above-mentioned simulations the transitions cease at a much closer radius than we assume here. The formula shown in the second row of Table 1 summarizes our model for the anisotropy profile.

4.3. Potential $\Phi(r)$

The next quantity required for the σ_r modeling is the potential, $\Phi(r)$. We essentially construct a model of the Galactic potential with three components: an oblate spheroidal bulge, an axisymmetric disk described by Miyamoto & Nagai (1975), and a spherical dark halo described by a ΛCDM motivated Navarro–Frenk–White (NFW; Navarro et al. 1996) profile. The formulae are given in Table 1.

The Galactic dark matter halo assumed to follow an NFW profile is characterized by two parameters, the virial mass M_{vir} and the concentration c (third row of Table 1). Here the overdensity of the dark matter compared to the average matter density, δ_{th}, is considered to be 340 (Bryan & Norman 1998). The values for Hubble constant $H_0 = 70.4$ kms^{-1} Mpc^{-1} and the matter density of the universe $\Omega_m = 0.3$ are taken from Komatsu et al. (2011);[4] in other words, we assume that the mean density is $\Omega_m\delta_{\text{th}}$ times the cosmological critical density.

---

[4] Recently, the Planck Collaboration has revised the value of H_0 downward to 67.3 kms^{-1} Mpc^{-1} (Planck Collaboration et al. 2013). However, we still use the WMAP7 result from Komatsu et al. (2011) for an easy comparison with previous works.

Table 1
Model Prescription of the Assumed Components of the Galaxy

Physical Quantity	Model	Comments
	Stellar Halo	
Density	$\rho(r) \propto \begin{cases} (r/r_b)^{-2.4} & \text{if } r < r_b \\ (r/r_b)^{-4.5} & \text{if } r_b \leqslant r < r_t \\ (r_t/r_b)^{-4.5}(r/r_t)^{\epsilon}\exp\left[-\frac{r-r_t}{\Delta}\right] & \text{if } r \geqslant r_t. \end{cases}$	r_b is the break radius, r_t is the truncation radius, and Δ is the scale length of fall. Assuming that the logarithmic slope at $r = r_t$ is continuous gives $\epsilon = \frac{r_t}{\Delta} - 4.5$.
Anisotropy	$\beta(r) = \begin{cases} \text{Interpolate(observed values)} & \text{if } r \leqslant 25\text{ kpc} \\ \begin{cases} \text{Max}\{\frac{r-25}{r_2-25}\beta_s, \beta_s\} & \text{if } \beta_s < 0 \\ \text{Min}\{\frac{r-25}{r_2-25}\beta_s, \beta_s\} & \text{if } \beta_s \geqslant 0 \end{cases} & \text{if } r > 25\text{ kpc} \end{cases}$	Observed values are taken from the literature (Kafle et al. 2012; Deason et al. 2013), 25 is maximum observed distance in kiloparsecs, β_s is the velocity anisotropy outside radius r_2.
	Dark Halo	
NFW potential (Navarro et al. 1996)	$\Phi_{\text{NFW}} = \frac{-GM_{\text{vir}}\ln(1+rc/R_{\text{vir}})}{g(c)r},$ $g(c) = \ln(1+c) - \frac{c}{1+c}, \quad$ and $R_{\text{vir}} = \left(\frac{2M_{\text{vir}}G}{H_0^2\Omega_m\delta_{\text{th}}}\right)^{1/3}$	M_{vir}, c, and R_{vir} are the virial mass, concentration, and the virial radius, respectively. δ_{th} is an overdensity of the dark matter compared to the average matter density, H_0 is the Hubble constant, and Ω_m is the matter density of the universe.
	Disk	
Miyamoto & Nagai (1975) potential	$\Phi_{\text{disk}}(R, z) = -\frac{GM_{\text{disk}}}{\sqrt{R^2 + (a + \sqrt{z^2+b^2})^2}}$	a, b, and M_{disk} are the scale length, scale height, and mass, respectively.
	Bulge	
Spheroidal bulge (Binney & Tremaine 2008, Equations (2.207a) and (2.207b)) density	$\rho_{\text{bulge}}(R, z) = \rho_{b0}\left(\frac{m}{a_b}\right)^{-\alpha_b}e^{-m^2/s^2}, \quad$ where $m = \sqrt{R^2 + z^2/q_b^2}$	ρ_{b0} is a density normalization, which is a function of M_{bulge}. s is a scale length. Values for remaining parameters a_b, α_b, and q_b are assumed to be 1 kpc, 1.8, and 0.6, respectively, and are adopted from Section 2.7, page 111, of Binney & Tremaine (2008).

The Galactic disk is thought to have two major components, i.e., a thick and a thin disk (e.g., Gilmore & Reid 1983). Generally, the disk is modeled as exponential in a sense that the surface density falls exponentially as a function of distance from the center of the Galaxy R and height from the Galactic midplane z. Since here we use the spherical Jeans equation, we consider an analytic and easy-to-use three-dimensional model of the disk, which is provided by a flattened disk of Miyamoto & Nagai (1975) type. Its functional form is given in the second-to-last row of Table 1. There, a and b are its scale lengths and M_{disk} is the mass.

The Galactic bulge is assumed to be spheroidal. This provides a reasonable axisymmetric approximation for the bulge seen from *COBE*/DIRBE near-infrared data. It is also similar to the axisymmetric approximation of the Bissantz & Gerhard (2002) model considered in McMillan (2011). The last row of Table 1 presents the mass density of the assumed model for the bulge and is taken from Equations (2.207a) and (2.207b) in Binney & Tremaine (2008). To compute the force generated by such a spheroidal system, we use Equations (2.129a) and (2.129b) of Binney & Tremaine (2008). The values for some of the bulge parameters are kept fixed, such as oblateness parameter q_b and power-law index α_b. These were adopted from Section 10.2.1 of Binney & Merrifield (1998). We found that at a distance greater than four times the scale length s, the spheroidal bulge contribution to the overall potential is similar to that of a point mass.

Both the disk and bulge models are functions of radius and polar angle. But here we work in a framework of the spherical Jeans equation. Hence, we only consider the radial component of the force due to disk and bulge, i.e., along the basis vector $\widehat{e_r}$, which we average over the spherical shells. The average force exerted on a unit mass at given radius r due to all three components of the Galaxy is modeled by

$$\frac{d\Phi(r)}{dr} = \langle\nabla\Phi_{\text{bulge}}(R, z).\widehat{e_r}\rangle + \langle\nabla\Phi_{\text{disk}}(R, z).\widehat{e_r}\rangle + \frac{d\Phi_{\text{NFW}}(r)}{dr}. \tag{10}$$

The dominant contributor to the overall potential of the Galaxy in the innermost region $r \lesssim 5$ kpc is the bulge, in 5 kpc $< r <$ 15 kpc is the disk, and at even larger distances is the halo. Therefore, fixing a potential of any component would systematically alter the contribution of the others. Thus, we keep the parameters free and allow the data to resolve the degeneracies.

Before proceeding with the fit, we first study the effect of density and anisotropy profiles in the $\sigma_r(r)$ model. The model $\sigma_r(r)$ is obtained by substituting the above-described density, anisotropy, and potential profiles in Equation (9). In Figure 3(a), we demonstrate the role of the assumed density profile for the case of $\beta = 0.5$, $c = 10$, and $M_{\text{vir}} = 10^{12} M_\odot$. The solid (dotted) line is the case of a single power law with a slope of 2.4 (4.5), whereas the dashed line is the case of a double power-law density profile with an inner slope 2.4 and an outer slope 4.5, with the break being at $r_b = 50$ kpc. In the figure the σ_r for the double power-law case attains the values for single power-law cases in the inner and outer parts with a sharp transition ceasing exactly at the break radius r_b. Furthermore, the dashed-dotted line in the figure is the same as in the case of the dashed
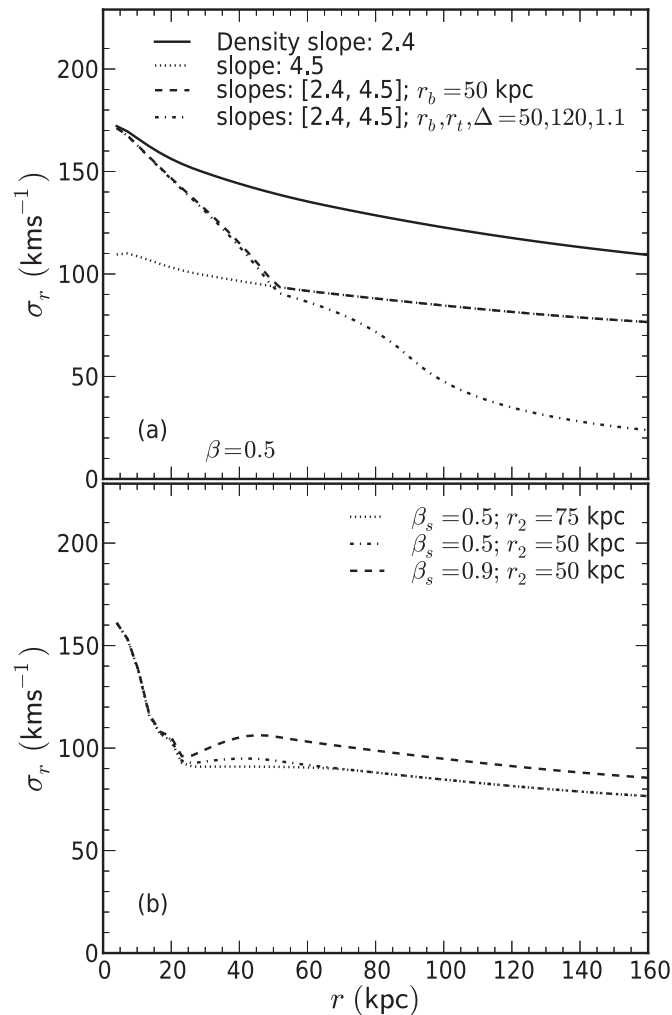
Figure 3. Effect of density and anisotropy parameters in the σ_r model: (a) shows an effect of assumed density power laws for the case of constant β, c, and M_{vir}; and (b) shows an effect of assumed β profile and its parameter r_2 and β_s for the case of double power-law density and constant c and M_{vir}. In all cases bulge and disk parameters are kept fixed as $M_{disk} = 10^{11} M_\odot$, $a = 4.5$ kpc, $b = 0.8$ kpc, $M_{bulge} = 10^{10} M_\odot$, $s = 1.9$ kpc, $a_b = 1$ kpc, $\alpha_b = 1.8$, and $q_b = 0.6$.

line but with an exponential fall-off beyond $r_t = 120$ kpc with parameter $\Delta = 1.1$ kpc. Note that the σ_r for the dashed-dotted line and dashed line cases are the same out to $r_b = 50$ kpc, but beyond that the dashed-dotted line declines further owing to added exponential fall-off in the density profile. Since the slope in the latter case is a function of r, the transition is smoother than one near the first break r_b. For $r > r_t$, σ_r decreases gently. This suggests that the break in the $\sigma_r(r)$ profile is a result of the break, r_b, in the density distribution.

In Figure 3(b), we demonstrate the effect of the underlying β profile for the case of $c = 10$, $M_{vir} = 10^{12} M_\odot$, density power-law index of 2.4 (inner region) and 4.5 (outer region), and $r_b = 23$ kpc. The $\beta(r)$ plotted here are taken from the second row of Table 1. The dotted line and dashed-dotted lines show $\beta(r)$ with $\beta_s = 0.5$ and $r_2 = 75$ kpc and 50 kpc, respectively. These two runs can be compared to see the effect of r_2 on the $\sigma_r(r)$ model. Clearly, the chosen value of r_2 that determines the distance at which β saturates and attains constant β_s value is just the measure of the slope of the transition. Also, as expected, in the case of $r_2 = 75$ kpc the slope is smaller than in the case of $r_2 = 50$ kpc as it attains the β_s at larger r. The effect of r_2 seems

minimal in the overall $\sigma_r(r)$ profile. Hence, we keep it fixed at 50 kpc for the rest of the analysis. Furthermore, the above two runs can be compared with the dashed line to see the effect of adopted β_s, which is 0.5 in the former runs and 0.9 in the latter one. As expected, larger $\beta_s = 0.9$ means that the $\sigma_r(r)$ shifts up and vice versa. The β_s can systematically shift the $\sigma_r(r)$ profile and bias the mass estimate; we keep it free.

The model parameters we are interested in measuring are the stellar halo density power-law break radius (r_b), truncation radius (r_t), truncation softening (Δ), and maximum anisotropy (β_s); dark matter halo concentration (c) and the virial mass (M_{vir}); disk scale lengths (a and b) and mass (M_{disk}); and bulge scale length (s) and mass (M_{bulge}). We consider flat priors for all the parameters in the following range: $r_b \in [8, 30]$ kpc, $r_t \in [60, 140]$ kpc, $\Delta \in [0, 20]$ kpc, $\beta_s \in [-5, 1]$, $c \in [1, 60]$, $M_{vir} \in [0.05, 3] \times 10^{12} M_\odot$, $M_{disk} \in [0.1, 5] \times 10^{11} M_\odot$, $a \in [0.1, 12]$ kpc, $b \in [0.01, 0.5]$ kpc, $M_{bulge} \in [0.1, 3] \times 10^{10} M_\odot$, and $s \in [1, 3]$ kpc.

Next, we use the MCMC and likelihood maximization to compute the model parameters of interest. The likelihood function we use is

$$L(\theta|\text{Data}) = p(\theta|p(\sigma_r|r))p(\theta|v_{\text{term}}, l, \sigma_{v_{\text{term}}})p(\omega_{\text{LSR}}(\theta)),$$

where $\theta = \{r_b, r_t, \Delta, \beta_s, c, M_{vir}, M_{disk}, a, b, M_{bulge}, s\}$ is the set of model parameters we explore. The last term is the prior on ω_{LSR}. The first term is

$$p(\theta|p(\sigma_r|r)) = \prod_{k=1}^{m} p(\sigma_r(r_k, \theta)|r_k). \quad (11)$$

In this model $\sigma_r(r_k, \theta)$ is given by Equation (9). The probability $p(\sigma_r|r_k)$ is the posterior distribution of σ_r parameter at the kth node and is obtained from Equation (8) in Section 3, in other words, the distribution of each data point in Figure 1. This setup avoids assuming gaussian errors for the measured values; instead, we already have the full probability distribution of σ_r at each r, and we make use of this.

Our catalog only contains the halo stars, and with the halo stars alone we cannot construct the rotation curve for the inner region of the Galaxy. Fortunately, the shape of the rotation curve or the circular velocity v_{circ} in the innermost region of the Galaxy $r < R_\odot$ kpc, where the bulge and the disk dominate, can be computed from alternative measures such as using tangent point velocities (e.g., Malhotra 1995; McClure-Griffiths & Dickey 2007) or the gas rotation curve (e.g., Sofue et al. 2009). Here we use the terminal velocity curves from Malhotra (1994, 1995), as done, e.g., in Dehnen & Binney (1998), Widrow et al. (2008), McMillan (2011).

By measuring the terminal velocity along all lines of sight between Galactic longitudes $|l| < \pi/2$ for latitude $b = 0°$, it is possible to derive a measurement of the rotation curve of the inner Galaxy. Assuming that the Galaxy is axisymmetric, v_{term} as a function of l is given by

$$v_{\text{term}}(l) = v_{\text{circ}}(R_\odot \sin l) - v_{\text{LSR}} \sin l, \quad (12)$$

where $v_{\text{LSR}} = v_{\text{circ}}(R_\odot)$. Now we define our second term in likelihood as

$$p(\theta|v_{\text{term}}, l, \sigma_{v_{\text{term}}}) = \prod_k \mathcal{N}(v_{\text{term}}(l_k, \theta)|v_{\text{term}}^k, \sigma_{v_{\text{term}}}^k, l^k). \quad (13)$$

There will be effects of nonaxisymmetry of the Galaxy and noncircular motion of the interstellar medium on the $v_{\text{term}}^{\text{data}}$.
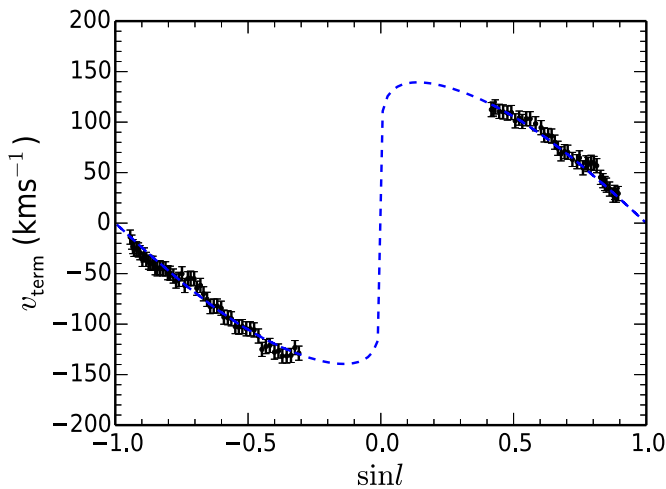
Figure 4. Terminal velocity v_{term} as a function of Galactic longitude l. The points are the data taken from Malhotra (1994, 1995). The error bars of 7 km s^{-1} shown are introduced to allow for noncircular motions. The overplotted line is our best-fit model resulting from our final MCMC run corresponding to Figure 6.

(A color version of this figure is available in the online journal.)

Figure 5. Angular velocity (ω) at $R_\odot$. The black histogram shows the posterior distribution of ω obtained from the MCMC run for the case with uniform prior. The best-fit value of ω is 30.2 ± 1.2 km s^{-1} kpc^{-1}. The blue dotted line is the normal distribution with a mean value of 28.8 km s^{-1} kpc^{-1} and a dispersion of 0.2 obtained for $V_\odot = 12.24$ km s^{-1} and $R_\odot = 8.5$ kpc from Reid & Brunthaler (2004), which we later use as a prior.

(A color version of this figure is available in the online journal.)

To take into account these effects, following Dehnen & Binney (1998), we assume $\sigma_{v_{term}} = 7$ km s^{-1} and avoid the region affected by the bar by only using data with $|\sin l| > 0.3$. The data with assumed uncertainties are shown with black points in Figure 4.

An additional prior we impose is on v_{LSR}. There is a wide variation in claims about v_{LSR} at $R_\odot$ ranging between 184 km s^{-1} (Olling & Merrifield 1998) and 272 km s^{-1} (Méndez et al. 1999). Many of these claims depend on the assumed $R_\odot$ and are normally measured using the data within the solar annulus. In their studies of masers, McMillan & Binney (2010) find that the angular velocity is constrained better ranging between 29.9 and 31.6 km s^{-1} kpc^{-1}. As a summary of all these works, we assign a prior with a uniform distribution of

$$p(\omega_{LSR}) = \mathcal{U}(23, 34). \qquad (14)$$

The range in ω_{LSR} of [23, 34] km s^{-1} kpc^{-1} corresponds to a range in v_{LSR} of [196, 289] km s^{-1} at $R_\odot = 8.5$ kpc.

We have the σ_r run for two different tracers, i.e., giant and BHB stars, labeled with red and black in Figure 1. While the σ_r run of the giant data is measured out to a larger distance ($r \sim 155$ kpc) than of the BHB stars ($r \sim 40$ kpc), the giant stars have comparatively larger uncertainties in r and $\sigma_r(r)$ than BHB stars. Importantly, the $\beta(r \leqslant 25$ kpc) profile that goes into our modeling is also unknown for the giant data but known for the BHB data. It is therefore more sensible to take the best portion of the data in hand and combine them. Therefore, for our final round of measurements, we take an adjoined $\sigma_r(r)$: the BHB data from K12 in the range $12 \lesssim r/\text{kpc} \lesssim 40$ and the giant star data in the range $40 \lesssim r/\text{kpc} \lesssim 155$. Note that our model for the $\sigma_r(r)$ (see Figure 3) does not predict the flattening out of the profile in the inner region $r \lesssim 12$ kpc. However, the first two $\sigma_r(r)$ values in the figure for the BHB sample show a clear flattening. This is something that needs to be investigated in the future; currently we ignore these data points.

During an MCMC run, for every proposed set of values of model parameters, particularly one defining the potentials, we get a prediction for ω_{LSR} (shown in Figure 5 by a hatched histogram). We are able to constrain the $\omega_{LSR} = 30.2 \pm 1.2$ km s^{-1} kpc^{-1}. Interestingly, this is within the

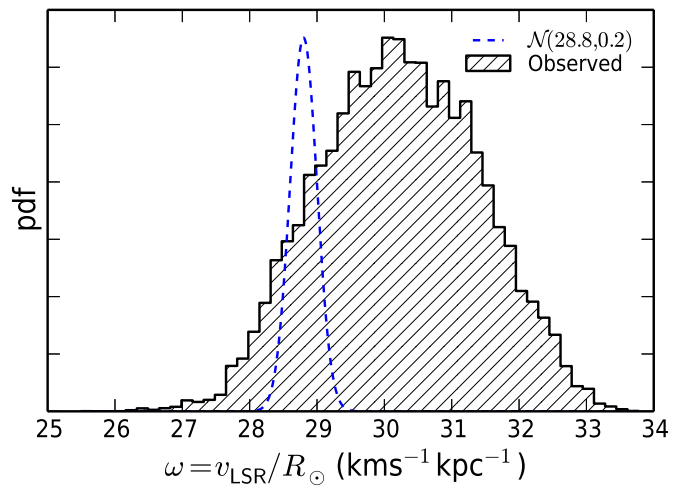uncertainty range of the Reid & Brunthaler (2004) result 28.8 ± 0.2 km s^{-1} kpc^{-1} for $V_\odot = 12.24$ km s^{-1} obtained using the Sgr A*'s proper motion. Also, our estimate falls in the prescribed range 29.9–31.6 km s^{-1} kpc^{-1} in McMillan & Binney (2010), who use the proper motions of masers. Our measurement therefore can be taken as an independent measurement of the v_{LSR} at $R_\odot = 8.5$ kpc. Since our constraint of ω_{LSR} has larger uncertainties compare to the one obtained using Sgr A* data, from here on unless otherwise mentioned we use $\mathcal{N}(\omega_{LSR}|28.8, 0.2)$ as a prior instead of a uniform distribution.

5. RESULTS AND DISCUSSION

Figure 6 displays the marginalized one- and two-dimensional distributions obtained from the MCMC. For a quick referral the table with the best-fit estimates is put alongside the figure. It is also summarized separately in Table 2 for both cases, i.e., with and without Sgr A* proper motion prior. The reported best-fit values are the medians of the posterior distributions of the model parameters, whereas the uncertainties quoted are computed from 16th and 84th percentile values. The best-fit σ_r model obtained after substituting the above estimates is shown, against the actual data, by a black dashed line in Figure 1. It can be seen that the best fit represents the data well. A small rise in $\sigma_r(r)$ data at $r = 70$ kpc seems to be a local effect and could be due to the presence of some kind of shell-like structure at the given distance. For a proper fitting of such outliers we need to know the underlying $\beta(r)$ run of the data.

Figure 6 nicely demonstrates correlations that exist among different parameters we consider here. For example, one can observe an expected correlation between β_s and M_{vir}, also known as *the mass-anisotropy degeneracy*. Also, one can see a mild correlation between M_{bulge} and M_{disk}, M_{vir} and M_{disk}, etc. An anticorrelation is seen between c and M_{disk} and M_{bulge}.

The best-fit estimates of the model parameters enable us to construct the rotation curve of the Galaxy (shown in Figure 7). The dashed, dotted, and dashed-dotted lines are the $v_{circ}(R)$ as a function of the cylindrical radius R for the halo, disk, and bulge, respectively, whereas the solid line is the resultant curve.
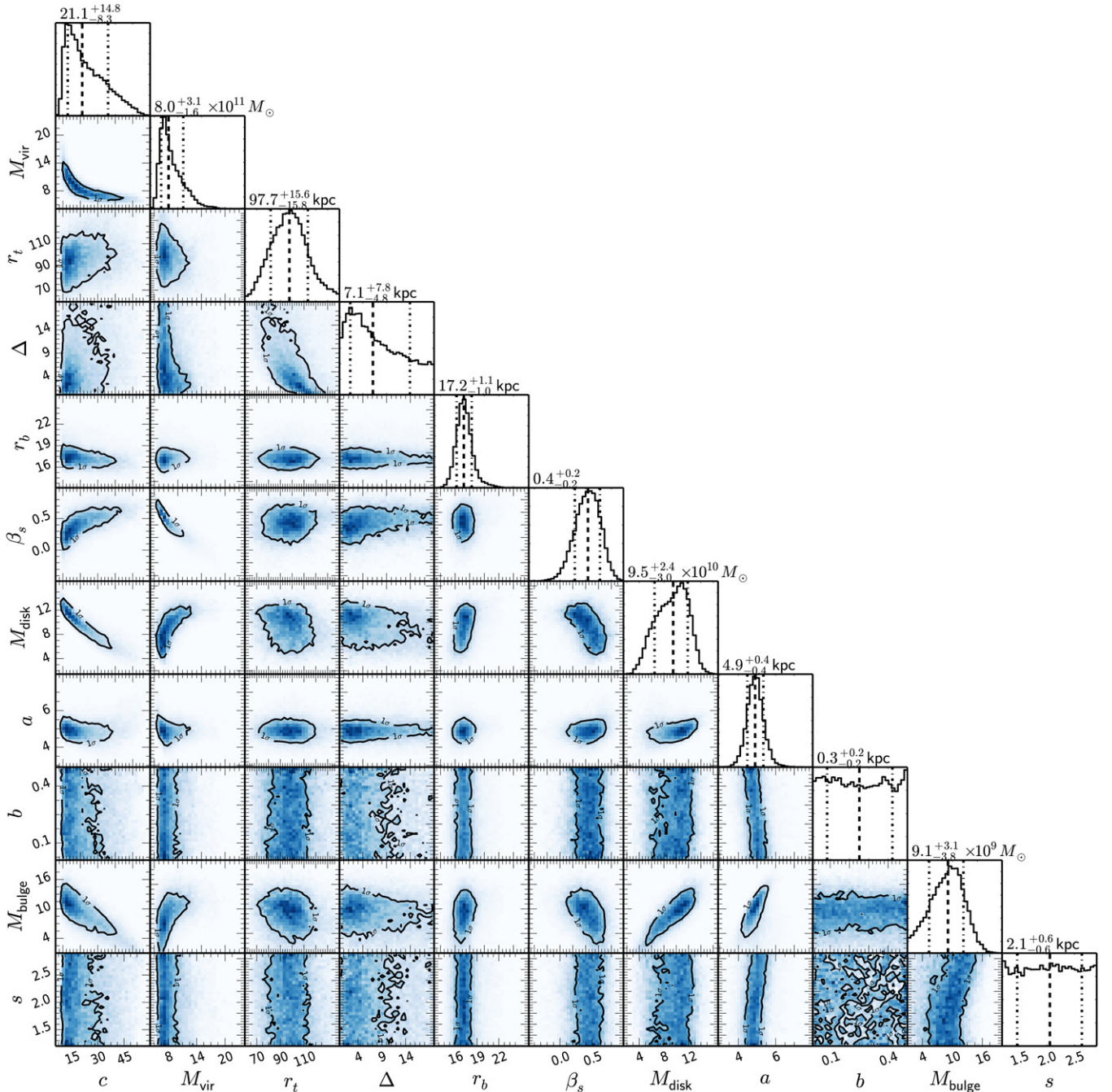
Figure 6. Joint likelihood and the marginal posterior distributions of the model parameters obtained from the MCMC exploration of the combined sample of the halo giant and BHB stars. The labels along the horizontal and vertical direction tell the names of the parameters, i.e., from the left to the right they are the NFW dark matter halo concentration c, virial mass M_{vir} in $10^{11} M_{\odot}$, density break radius r_b in kiloparsecs, truncation radius r_t in kpc, truncation softening parameter Δ, anisotropy β_s, disk mass M_{disk} in $10^{10} M_{\odot}$, disk scale length a in kiloparsecs, disk scale height b in kiloparsecs, bulge mass M_{bulge} in $10^9 M_{\odot}$, and bulge scale length s in kiloparsecs. Histograms at the top of each column show the posterior distribution of the model parameters named at the bottom of the column, whereas the heat maps depict the joint likelihood distribution of two parameters named immediately below and on the leftmost end of the same row. Black lines mark the 1σ confidence contours. The values in the title of histograms present the best-fit estimates.

(A color version of this figure is available in the online journal.)

Substituting the best-fit rotation curve in Equation (12) gives us the best-fit terminal velocity curve. In Figure 4 it is plotted alongside the terminal velocity data.

5.1. Properties of Disk and Bulge

In this paper we use an Miyamoto–Nagai (MN) disk and a spheroidal bulge. The properties of the disk and the bulge are mainly governed by the terminal velocity data. They are also quite sensitive to the prior on v_{LSR}, which in turn depends

on the chosen value of $R_{\odot}$. Overall the disk mass is around $10^{11} M_{\odot}$ and the bulge mass is around $10^{10} M_{\odot}$. The structural parameters like b and s are difficult to measure. The bulge mass has a mild dependence on s, but other than that, b and s have little effect on other parameters (see Figure 6). We find that $a + b$ is well constrained by the data. This can be seen by the strong anticorrelation between them and a narrow spread around it. Our inability to measure b is due to the following two reasons. First, the priors from terminal velocity data and
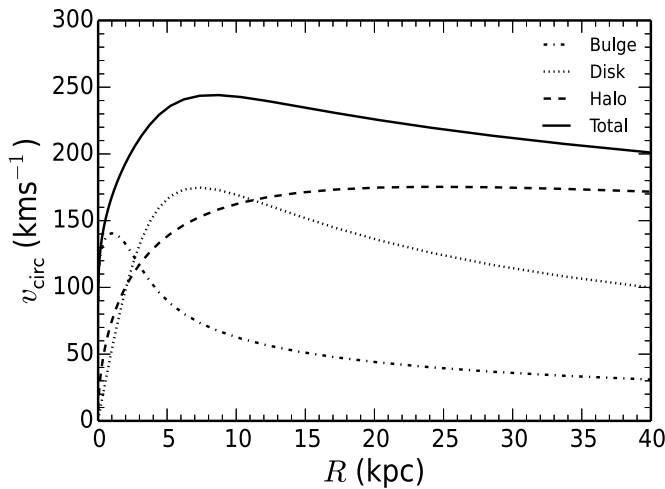
Figure 7. Circular velocity curve of the Galaxy. The dotted, dashed-dotted, and dashed lines are the circular velocity curves along the meridional plane, $z = 0$, for the oblate bulge, Miyamoto–Nagai (MN) disk, and NFW halo, respectively. The radius R is the distance in the Galactic plane. The individual curves are constructed from the best-fit estimates of the model parameters. The solid line shows the resultant circular velocity curves due to all three components of the Galaxy.

Table 2
Best-fitting Values of the Model Parameters

Galaxy Components	Parameter (unit)	Without v_{LSR} Prior	With v_{LSR} Prior
Stellar halo	r_b (kpc)	$17.5^{+1.2}_{-1.2}$	$17.2^{+1.2}_{-1.0}$
	r_t (kpc)	$100.4^{+17.7}_{-16.5}$	$97.7^{+15.6}_{-15.8}$
	Δ (kpc)	$8.3^{+7.5}_{-5.6}$	$7.1^{+7.8}_{-4.8}$
	β_s	$0.6^{+0.2}_{-0.2}$	$0.4^{+0.2}_{-0.2}$
Dark halo	c	$17.5^{+15.4}_{-7.5}$	$21.1^{+14.8}_{-8.3}$
	M_{vir} ($\times10^{12}\,M_\odot$)	$0.62^{+0.25}_{-0.21}$	$0.80^{+0.31}_{-0.16}$
Disk	M_{disk} ($\times10^{11}\,M_\odot$)	$1.5^{+0.6}_{-0.6}$	$0.95^{+0.24}_{-0.30}$
	a (kpc)	$5.8^{+0.6}_{-0.9}$	$4.9^{+0.4}_{-0.4}$
	b (kpc)	$0.2^{+0.2}_{-0.2}$	$0.3^{+0.2}_{-0.2}$
Bulge	M_{bulge} ($\times10^{10}\,M_\odot$)	$1.2^{+0.4}_{-0.5}$	$0.91^{+0.31}_{-0.38}$
	s (kpc)	$2.2^{+0.5}_{-0.6}$	$2.1^{+0.6}_{-0.6}$
Angular velocity	$\omega_\odot$ (km s^{-1} kpc^{-1})	30.2 ± 1.2	$\cdots$

Sgr A* we use basically provide $v_{circ}(R)|_{z=0}$, and this is sensitive only to the sum $a + b$. Second, in our setup the halo kinematics responds to forces averaged in radial shells, which decreases sensitivity to b.

Since b and s are not well determined by the data, the choice of prior becomes important for them. Traditionally, a double exponential form is used to fit the disk density. By fitting exponential disks to mono-abundance populations, Bovy et al. (2012) finds scale lengths to be roughly in the range 2–4.5 kpc and scale heights to be roughly in the range 0.2–1 kpc. Here we use an MN disk, so to facilitate comparison we derive the appropriate scaling factors. If we fit the surface density of an MN disk with an exponential form, for $2 < R/\mathrm{kpc} < 8.5$, we get a scale length of about $0.82a$. Fitting the density in the vertical direction, in the range $0.5 < z/\mathrm{kpc} < 2.0$ near the Sun, we get a scale height of $1.75b$. We adopt a uniform prior for b in the range 0–0.5 kpc, which is within the range expected for exponential disks. The value of a that we get is also within the range of expectation. For s we adopt a uniform prior in the
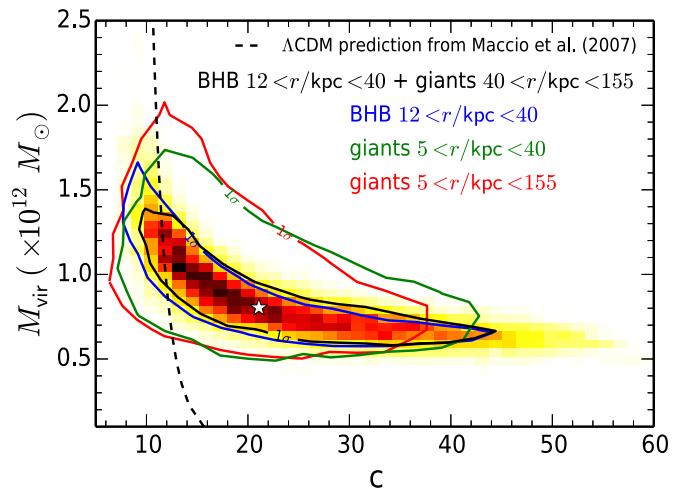

Figure 8. Concentration (c)–virial mass (M_{vir}) contours for $R_\odot = 8.5$ kpc. Red and green contours are for the giant star sample, the blue contour is for the BHB sample, and the black contour is for a combined sample of BHB and giant stars in a separate distance range as labeled in the figure. Solid lines depict the 1σ region. A white star denotes the best-fit estimate, and pixel plot shows a two-dimensional posterior distribution corresponding to the black contour. The black dashed line demonstrates a typical $c - M_{vir}$ relation predicted by ΛCDM dark matter simulation.

(A color version of this figure is available in the online journal.)

range 1–3 kpc, which is around the value 1.9 kpc as suggested by Binney & Tremaine (2008).

5.2. Anisotropy in the Outer Halo

Our best-fit estimate for the anisotropy in outer parts β_s is 0.4 ± 0.2. It is interesting that we are able to constrain β_s; the reason is as follows. In the innermost region, the terminal velocity data and prior on ω_{LSR} provide information about the bulge and also to some extent disk parameters. In the region $12 < r/\mathrm{kpc} < 25$ the BHB anisotropy is already known and the kinematics when put in the Jeans equation provides estimates for r_b, M_{vir}, c, and disk parameters. Now, beyond $r > 25$ kpc where β_s is introduced, it is in some sense the only unknown.

5.3. Mass and Concentration of Dark Matter Halo

We estimate the mass of the dark matter halo to be $M_{vir} = 0.80^{+0.31}_{-0.16} \times 10^{12}\,M_\odot$ and the concentration $c = 21.1^{+14.8}_{-8.3}$. Corresponding values for the virial radius R_{vir} and virial velocity are found to be $239.1^{+27.6}_{-16.6}$ kpc and $120.2^{+13.9}_{-8.3}$ km s^{-1}, respectively. It can be seen in Figure 8 that there is a strong anticorrelation between c and M_{vir}. The upper bound on c is not as well constrained as the lower bound. Simulated virialized halos in ΛCDM cosmology, in general, predict an inversely proportional relation between their mass and concentration (e.g., Bullock et al. 2001; Macciò et al. 2007; Duffy et al. 2008; King & Mead 2011). The dashed line in Figure 8 shows one such relation, $c = 327.3\,M_{vir}^{-0.12}$, adopted from Macciò et al. (2007). We see that the prediction of the ΛCDM simulation for the dark matter halo in the range $10^{11} \leqslant M_{vir}/M_\odot \leqslant 10^{13}$ passes through our measurements. However, note that the predictions are for pure dark matter simulations and do not include baryonic processes such as cooling, star formation, and feedback. The collapse of gas due to cooling leads to adiabatic contraction of the dark matter halo, which increases its concentration. Feedback, on the other hand, can have the reverse effect. Therefore, it is difficult to comment whether the concentration we get is typical or atypical of the Milky-Way-sized galaxies.

5.4. Do the Kinematics of the Giant and BHB Stars Result in a Consistent Galactic Potential?

To answer this, we now run the MCMC separately over a subset of our sample of the halo giant and the BHB samples taken from Figure 1. We select BHB and giant stars in a common radial range, i.e., $r \lesssim 40$ kpc. For the BHB sample we estimate $c = 22.8^{+12.1}_{-7.8}$ and $M_{\rm vir} = 0.74^{+0.18}_{-0.12} \times 10^{12}\, M_\odot$, whereas for the giant sample we estimate $c = 20.4^{+13.8}_{-8.9}$ and $M_{\rm vir} = 0.90^{+0.46}_{-0.26} \times 10^{12}\, M_\odot$. The $c - M_{\rm vir}$ joint-likelihood distributions for the above two data sets are shown by the blue and green contours in Figure 8, respectively. The distributions for both samples seem to be in good agreement, except for the fact that it is more puffed for giants than the BHB sample. We find that this is mainly due to larger uncertainties in the $\sigma_r(r)$ values for the giants in comparison with the BHB sample, which we verified by swapping the error bars in BHBs and giants. To conclude, the kinematics of the two halo populations, namely, BHBs and giants, are consistent with the fact that they both feel the same Galactic potential, at least within the radius $r \lesssim 40$ kpc.

5.5. Break in Slope of Stellar Halo Density Profile

Kinematics of halo stars allow us to constrain the density profile of the halo. We had modeled the density profile in the inner region by a double power law with fixed slopes, but the location of the break radius was kept free. For BHBs we measure r_b to be $17.1^{+1.2}_{-1.0}$ kpc, and for giants we measure it to be $22.1^{+4.1}_{-3.1}$ kpc. A reason for the different r_b for these two halo populations could be the uncertainties in the distances, which are larger for the giants than for the BHBs. Our estimate for the break radius is slightly smaller than $\sim$27 kpc as claimed in Deason et al. (2011) or $\sim$25 kpc as found in Watkins et al. (2009). Interestingly, our estimates are in good agreement with the recent study of RR Lyrae stars in Sesar et al. (2013), who suggest a break in the power law at a much smaller radius of $\sim$16 kpc. A smaller break radius also complies with the study of SDSS main-sequence turnoff stars in Bell et al. (2008), who conclude that the slope of the density profile at $r \lesssim 20$ kpc should be shallower in comparison with the radius outside this range. Here, a point worth noting is that our estimate of the break radius is linked to the kinematic features, whereas all the above values from the literature are inferred from the studies of the spatial distribution.

5.6. What More Do We Learn from the Tracers Extending Out to the "Edge" of the Galactic Halo?

To find an answer, we now run the MCMC hammer over the halo giant stars spanning $5 \lesssim r/{\rm kpc} \lesssim 155$. The red contour in Figure 8 shows the corresponding $c - M_{\rm vir}$ joint distribution, which is found to almost coincide with the green contours obtained for a giant catalog with $r \lesssim 40$ kpc. Similarly, a comparison of the blue contour in the figure, which is for the BHB sample within $12 \lesssim r/{\rm kpc} \lesssim 40$, with the black contour, which is for a combined sample of BHB and giant stars in distance ranges $12 \lesssim r/{\rm kpc} \lesssim 155$, shows that they are similar. This suggests that the giant data in the range $40 < r/{\rm kpc} < 155$ do not add much to our knowledge of c and $M_{\rm vir}$, i.e., the potential of the Galaxy. This is mainly due to our adoption of a parameterized form for the distribution of dark mater, namely, the NFW profile. The NFW profile predicts that for $r \gg R_{\rm vir}/c$ the density falls as r^{-3}. Therefore, data that extend out to about two times the scale radius $R_{\rm vir}/c$ should be sufficient to constrain

the two independent parameters $M_{\rm vir}$ and c of the NFW profile. However, if one wants to really compute the density out to the virial radius, e.g., by nonparametric schemes, then kinematic data till the virial radius would be required. In our case the distant giant stars ($r > 40$ kpc) turn out to be useful to probe the density distribution of the tracer population, i.e., the stellar halo. We find $r_t = 97.7^{+15.6}_{-15.8}$ kpc and $\Delta = 7.1^{+7.8}_{-4.8}$ kpc. It is interesting to note that the hydrodynamical simulations (e.g., Abadi et al. 2006) to investigate the properties of luminous halos surrounding isolated galaxies do not predict a truncated halo; rather, they find that the halo extends to the virial radius. In the future, our results regarding the density profile of the outer stellar halo should be useful for testing theories of stellar halo formation. Recently, Deason et al. (2014), using A-type stars from SDSS, find a sudden drop in density profile of the stellar halo as traced by BHBs and blue stragglers, lending further support to our kinematics detection of such a drop.

5.7. Repercussions of the Lighter Halo

The number of subhalos of a given mass scales directly with the host halo mass (Springel et al. 2008). Therefore, an accurate estimate of the Galaxy mass has importance in understanding *the missing satellite problem*. One interpretation of the problem (Kauffmann et al. 1993; Klypin et al. 1999; Moore et al. 1999; Bullock 2010) is that the ΛCDM paradigm predicts a larger number of massive subhalos for the Milky-Way-sized halo (e.g., Boylan-Kolchin et al. 2011). The problem can be solved if the mass of the Galaxy is low. Figure 5 in Wang et al. (2012) allows us to directly compare the host halo mass with the probability of containing three or less than three subhalos with $v_{\rm max} > 30$ km s^{-1} (maximum value of the circular velocity). The relation is inferred from the studies of the halos obtained from the Millennium Simulation series, Aquarius and Phoenix projects. For a direct comparison we scale our measurement of c, $M_{\rm vir}$ to compute the mass M_{200} interior to r_{200} from the center of the halo, at which the mean density is 200 times the critical density. We obtain $M_{200} = 0.72^{+0.24}_{-0.13} \times 10^{12}\, M_\odot$ and corresponding concentration $c_{200} = 16.2^{+11.6}_{-6.7}$. Figure 5 in Wang et al. (2012) suggests that for the mass equal to our M_{200} there is $\sim$70% probability that the Galaxy should host three or less than three subhalos with $v_{\rm max} > 30$ km s^{-1}. Interestingly, from observations it is known that there are only three brightest satellites of the Galaxy, namely, the Small Magellanic Cloud, Large Magellanic Cloud, and Sagittarius dwarf have $v_{\rm max} \sim 30$ km s^{-1}. This at least suggests that there is no discrepancy between the observed number of luminous satellites with $v_{\rm max} > 30$ km s^{-1} and the number predicted by ΛCDM. Furthermore, Vera-Ciro et al. (2013) also concludes that for Milky Way mass $\sim 8 \times 10^{11}\, M_\odot$, which is similar to our mass, the number and internal dynamics of the dwarf spheroidal satellites of our Galaxy are consistent with the predictions of the ΛCDM model. Therefore, we remark that the scarcity of massive subhalos is not a failure of the ΛCDM paradigm but a repercussion of assuming higher virial mass for the Galaxy.

Another impact of the Galaxy mass is in describing the overall dynamics of the orbiting satellite galaxies. For our low estimate of Galaxy mass, are the satellites still bound is a natural question to ask. To study this, we measure the escape velocity $v_{\rm esc}$ using

$$v_{\rm esc}(r) = \sqrt{2|\Phi(r)|}, \qquad (15)$$

where

$$\Phi(r) = \langle \Phi_{\rm bulge}(R, z) \rangle + \langle \Phi_{\rm disk}(R, z) \rangle + \Phi_{\rm NFW}(r).$$
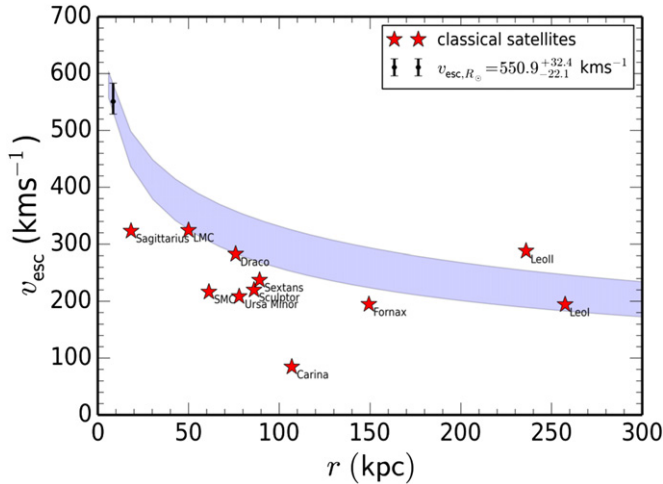
Figure 9. Escape velocity of the Galaxy. The observed escape velocity v_{esc} of the Galaxy is shown as a function of the galactocentric distance r. The v_{esc} at $R_\odot$ is shown by a black dot with error bar. Red stars shows the total velocities for the named Milky Way classical satellite galaxies adopted from Table 1 of Pawlowski & Kroupa (2013).

(A color version of this figure is available in the online journal.)

Figure 10. Cumulative mass of the Galaxy. The shade shows the observed mass of the Galaxy $M(< r)$ as a function of the galactocentric distance r. The black dot with error bar is the Law et al. (2005) estimate of the Galaxy mass within 50 kpc obtained by modeling the Sagittarius dwarf spheroidal galaxy tidal streams, whereas the diamond point is mass within $r < 60$ kpc obtained by Newberg et al. (2010) by modeling the Orphan Stream.

(A color version of this figure is available in the online journal.)

Our estimate of v_{esc} as a function of the galactocentric radius r is shown in Figure 9. The stars in the figure show the total velocities for the named Milky Way satellite galaxies. The velocities are computed from a recent compilation tabulated in Table 1 of Pawlowski & Kroupa (2013). Also, the velocities are corrected for our assumption of the velocity of the local standard of rest, i.e., 245 km s^{-1} at $R_\odot = 8.5$ kpc, except Leo II, which seems to be marginally unbound. We can conclude from Figure 9 that all the given satellites are bound despite our low estimate for the Galaxy mass.

In Figure 10 we present the cumulative mass $M(< r)$ of the Galaxy. It is computed using the formula for the centrifugal equilibrium

$$M(< r) = \frac{r^2}{G}\frac{d\Phi}{dr},$$

where $d\Phi/dr$ is taken from Equation (10) and uses spherical averaging. Infalling satellites are destroyed by their host's gravitational potential, resulting in tidal streams. Attempts to model these streams (Newberg et al. 2010; Law & Majewski 2010; Carlin et al. 2012) also provide an alternate constraint on the Galaxy mass. In Figure 10 the black dot with error bar is the Law et al. (2005) estimate of the Galaxy mass within 50 kpc obtained by modeling the Sagittarius dwarf spheroidal galaxy tidal streams. It is interesting to note that our estimate given the range of uncertainty agrees well with this result. However, the diamond point, which is mass within $r < 60$ kpc obtained by Newberg et al. (2010) by modeling the Orphan Stream, is significantly smaller than our prediction. One possible reason could be that they model the orbit and not the stream, and the possible misalignment between stream and orbit could bias the result (Sanders & Binney 2013a).

5.8. Local Constraints on Mass Density, Surface Density, and Escape Velocity

The local (at $R_\odot$) dark matter density provides a strong basis for the experimental endeavors for indirect detection of the dark matter; see Strigari (2013) for a review of the topic. Therefore, determination of the local mass distribution, the work originally pioneered by Oort (1932), has recently received a great deal
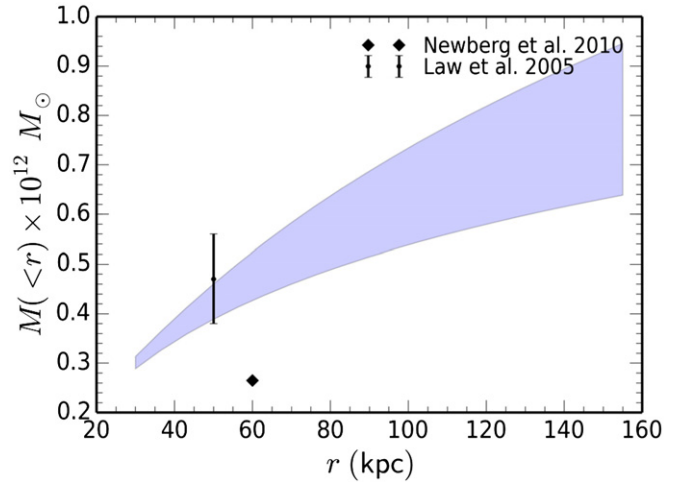
of attention. Our best-fit model of the halo potential allows us to compute the local dark matter density $\rho_\odot^{DM}$, which we measure to be $\rho_\odot^{DM} = 0.0088^{+0.0024}_{-0.0018}$ $M_\odot$ pc^{-3}, equivalent to $0.35^{+0.08}_{-0.07}$ GeV cm^{-3}. Our result is in good agreement with the recent estimates of 0.3 ± 0.1 GeV cm^{-3} by Bovy & Tremaine (2012), 0.40 ± 0.04 GeV cm^{-3} by McMillan (2011), or 0.389 ± 0.025 GeV cm^{-3} by Catena & Ullio (2010). However, we note slightly lower estimates of 0.007 $M_\odot$ pc^{-3} given in Holmberg & Flynn (2000), who utilize a catalog of A–F stars obtained from the *Hipparcos* survey and of 0.0065 ± 0.0023 $M_\odot$ pc^{-3} given in Zhang et al. (2013), who utilize K dwarf stars from SDSS/SEGUE.

Also, we measure the local escape velocity, using Equation (15), to be $v_{esc,R_\odot} = 550.9^{+32.4}_{-22.1}$ km s^{-1}. Our estimate seems to be slightly higher but within the range of uncertainties of 544^{+64}_{-46} km s^{-1} found using the high-velocity halo stars in Smith et al. (2007). Moreover, the most recent estimate of $v_{esc,R_\odot}$, again using the high-velocity stars, is provided to be 544^{+64}_{-46} km s^{-1} (Piffl et al. 2014). There $v_{esc,R_\odot}$ is defined to be the minimum speed required to reach three virial radii, where $R_{vir} = 180$ kpc. For a fair comparison we redefine Equation (15) to be equal to $\sqrt{2|\Phi(R) - \Phi(3R_{vir})|}$ and compute $v_{esc,R_\odot} = 528^{+24}_{-17}$ km s^{-1} for $R_\odot = 8.5$ kpc, which is in the lower range of quoted values in Piffl et al. (2014).

Yet another quantity of interest is whether our disk is maximal (Carignan & Freeman 1985; van Albada et al. 1985). A convention (Sackett 1997; Courteau et al. 2014) is that in a maximal disk 72% of the total rotational support v_{circ}^{total} is contributed by a disk v_{circ}^{disk}, i.e.,

$$F = \left(\frac{v_{circ}^{disk}(R_{max})}{v_{circ}^{total}(R_{max})}\right)^2 \gtrsim 0.72, \qquad (16)$$

where R_{max} is a radius at which $v_{circ}^{disk}(R)$ is maximum. For our model, we find $R_{max} = 7.4$ kpc and $F = 0.5$ or $v_{circ}^{disk}(R_{max})/v_{circ}^{total}(R_{max}) = 0.7$, i.e., at this radius 30% of the total rotational support is by a disk.

Because of a lesser contribution of the disk to the total rotation curve, we find the Galaxy disk at $R_{\rm max}$ to be submaximal. Recently, Bovy & Rix (2013), using SEGUE dwarfs, found a slightly higher value of $F = 0.69$ and concluded the disk to be maximal. They assumed an exponential disk, for which F is measured at $R = 2.2\,R_{\rm d}$ (scale length of the exponential disk). It is, however, interesting to note that in their studies of 12 out of 15 distant spiral galaxies, Kregel et al. (2005) find on average $F = 0.28$, which is nearly half of our estimate for the Galaxy.

Finally, we check whether the local (at $R_\odot$) column/surface density of our best-fit model is within an expected range. The surface density is computed using

$$\Sigma(R) = \int_{-1.1\ {\rm kpc}}^{1.1\ {\rm kpc}} \rho(R, z)\,dz. \tag{17}$$

The contribution of the disk to the surface density is strongly dependent on our prior for disk scale length b, so it is not really a prediction of our analysis. We find that $\Sigma_\odot^{\rm total}$ is $94.0^{+16.6}_{-20.3}\,M_\odot\,{\rm pc}^{-2}$. This is slightly higher than $71 \pm 6\,M_\odot\,{\rm pc}^{-2}$ obtained by Kuijken & Gilmore (1991) and $74 \pm 6\,M_\odot\,{\rm pc}^{-2}$ obtained by Holmberg & Flynn (2004), but within the range of large uncertainties we have. We note that recent measurements by Bovy & Rix (2013), Zhang et al. (2013), who use the kinematics of the SDSS/SEGUE dwarfs, suggest a slightly lower value of $\Sigma_\odot^{\rm total} = 68 \pm 4\,M_\odot\,{\rm pc}^{-2}$.

5.9. Systematics

The results presented here are potentially subject to systematic uncertainties such that the reader should be cautioned. We use fiducial isochrones for the distance estimation of the giants. But there might be systematics associated with them, and this will have an effect on our distance estimates. An independent way to validate our distance measurement would be to use an estimator shown in Schönrich et al. (2012), but this requires proper motions. It remains to be seen if any available proper motions of the distant giants are accurate enough for this method to be successfully applicable. Additionally, while measuring the distance to the halo K giants, we do not take into account uncertainties in the reddening estimate. We simply use colors dereddened according to Schlegel et al. (1998) extinction maps. This could introduce systematics in our distance estimate. However, we believe that such systematics, if any, would be insignificant. Firstly, the Schlegel et al. (1998) maps are accurate for high-latitude stars, and 98% of our sample has $|b| > 20°$. Secondly, although, Schlegel et al. (1998) maps provide total extinction, they are appropriate for halo stars as most of the dust is confined to the disk.

We use a sample of giants from SEGUE, which are subjected to a proper-motion restriction of 11 mas yr^{-1} (Yanny et al. 2009). This can potentially introduce a systematic bias for nearby giants, but the giants that we use for our main analysis are beyond 40 kpc, and for them the above-mentioned proper-motion limit safely includes all bound halo stars.

We assume that each tracer population is in Jeans equilibrium. In any case, it is important to note that we can determine the Galactic potential only to the extent that the phase-space distribution of tracer stars is in equilibrium (Binney 2013). However, if the tracer population under study is a superposition of multiple populations, then the Jeans equation should be applied separately for each population. In earlier studies with BHB stars (Kafle et al. 2013; Hattori et al. 2013), correlation between metallicity and kinematics of halo targets was found.

A similar correlation could exist for giants. So ideally, if one has a larger sample of stars, one should treat metal-rich and metal-poor populations separately. Moreover, close to the disk the potential is not spherically symmetric, so strictly speaking the spherical Jeans equation is not valid. This can potentially bias the estimate mass. This should be investigated in the future.

We model the disk by the MN form. In reality, the disk is described better by double-exponential functions. Moreover, the disk of the Milky Way is probably a superposition of multiple populations, each with different scale height and length. These facts can potentially bias our results. Finally, throughout our analysis we assume $R_\odot = 8.5$, and systematics due to our adopted value can be expected. Claims for a wide range in $R_\odot$ between ~7.7 and 8.8 kpc exist in the literature (e.g., Reid 1993; Nikiforov 2004; Gillessen et al. 2013; Francis & Anderson 2014; Reid et al. 2014, etc.). To study the influence of our adopted value of $R_\odot$, we reanalyze our data with $R_\odot = 8$ kpc. Firstly, we measure the $\sigma_r(r)$ run, which we find to be similar to one shown in Figure 1. Secondly, we run the MCMC model fitting to the above $\sigma_r(r)$ run. Assuming $R_\odot = 8$ kpc means that the prior in $v_{\rm LSR}$ changes, and this can have a significant influence in our measurement. It is mainly because we do not have halo data within $r \lesssim 12$ kpc, and the information about disk and bulge properties mostly comes from the assumption about $v_{\rm LSR}$ at $R_\odot$. We find that for $R_\odot = 8$ kpc our model parameters are $M_{\rm vir} = 1.2 \pm 0.3 \times 10^{12}\,M_\odot$, $c = 15.2^{+5.6}_{-3.2}$, $M_{\rm disk} = 0.71^{+0.11}_{-0.13} \times 10^{11}\,M_\odot$, $a = 3.0 \pm 0.6$ kpc, $M_{\rm bulge} = 0.70^{+0.31}_{-.32} \times 10^{10}\,M_\odot$, and $s = 2.1 \pm 0.6$ kpc, whereas r_b, r_t, Δ, and β_s remain unchanged.

Recall that our final results shown in Table 2 or Figure 6 are obtained for a combined sample of two halo populations, i.e., BHBs within a radius $r \lesssim 40$ kpc and giants outside $r \gtrsim 40$ kpc. As discussed earlier in Section 4.1, the density profile for same sample of BHB stars as ours is already computed in Deason et al. (2011), and this is what we assume in our analysis. In the region where giant star data is used we assume the density profile to be a power law with slope of -4.5, which is consistent with the findings for BHB (Deason et al. 2011) and RR Lyrae stars (Watkins et al. 2009). However, there is no direct measurement of the density of halo giants. Thus, to test the sensitivity of our results to the density profile, we run the MCMC simulation for two different values of slope indices, -4 and -5. From our fits we find that $M_{\rm vir}$ and c are directly proportional to the density slope. For each linear step of -0.5 from -4 to -5 we find that $M_{\rm vir}$ increases by ~30% for each step, whereas c increases by ~20%. For the same steps from -4 to -5, we find that $M_{\rm disk}$ and $M_{\rm bulge}$ decrease by ~22% and ~20%, respectively. Quantities such as r_b, r_t, Δ, and disk and bulge scale parameters remain unchanged. Moreover, the shape of the posterior distributions of the parameters and hence uncertainties remain the same for all the cases. It should be noted that the value of β_s remains nearly the same for both the cases, i.e., 0.5 ± 0.2 for -4 and 0.4 ± 0.2 for -5. This is not unexpected, as data in $12 < r/{\rm kpc} < 25$ for which observed β is available are enough to constrain $M_{\rm vir}$ and c. So any change in density profile affects the enclosed mass. When data beyond 25 kpc are added, the increase in power-law index is compensated by the increase in mass so as to leave β_s unchanged.

Before concluding, it is worth mentioning that we noted the parallel work by Bhattacharjee et al. (2014). It has some similarities with our works, e.g., uses of the Jeans equation, SDSS/SEGUE BHB and giant star catalog, etc. While estimating the mass using the Jeans equation, we note that they use the density

profile of the spectroscopic sample, which has a selection bias. In reality, the Jeans equation requires the underlying density profile of the tracers and not of the sample. Lastly, it has been found in the simulations that halo stars, satellites, and the dark matter halo have different orbital properties (Abadi et al. 2006; Sales et al. 2007). Hence, assuming a constant anisotropy for both field stars and satellites could introduce additional systematic uncertainties in their mass estimate. However, it should be noted that they do not model the disk, bulge, and halo separately, but only provide an estimate for the total mass $M(< r)$ within some radius.

6. CONCLUSION

A spectroscopic survey such as SEGUE provides us with a large catalog of distant and different tracer populations. Here we complemented the BHB star catalog (Xue et al. 2011) of the halo tracers with a catalog of K-giant stars. The position and line-of-sight velocities of these tracer populations, the terminal velocity curve, and the proper motion of the Sgr A* allow us to constrain the mass model and tracer properties of the Galaxy. This also allows us to break the degeneracy due to the varying relative contribution of the bulge-disk-halo to the rotation curve with the distance. Our presented estimates are the marginalized results over all possible values of anisotropy parameter and thus also take *the mass-anisotropy degeneracy* into account.

Our main results considering solar motion with respect to the local standard of rest as $U_\odot = +11.1$ km s^{-1}, $V_\odot = +12.24$ km s^{-1}, $W_\odot = +7.25$ km s^{-1} and its position from the center of the Galaxy at $R_\odot = 8.5$ kpc are summarized in Table 2 and discussed in Section 5. The following paragraphs highlight some of our main findings.

Stellar halo. The kinematics of the halo stars enables us to model the density profile of the stellar halo. We model the halo number density to be a double power law with an inner slope of -2.4 and an outer slope of -4.5 with a break occurring at radius r_b. We find $r_b = 17.2^{+1.1}_{-1.0}$ kpc. The break in the radial velocity dispersion profile is found to correspond to the break in the density. The mass estimate is found to be sensitive to the break radius r_b. The giant star data reveal that the outermost halo stars have a small velocity dispersion, but interestingly this suggests a truncation of the stellar halo density rather than a small overall mass of the Galaxy. We find that the stellar halo has an exponential truncation that starts at radius $r_t = 97.7^{+15.6}_{-15.8}$ kpc and has a scale length of $\Delta = 7.1^{+7.8}_{-4.8}$ kpc. Direct estimation of the density profile using photometry also seems to support the features in the density profile of the halo that we see using kinematics. For example, Sesar et al. (2013) using RR Lyrae report a break at $r_b = 16$ kpc, and Deason et al. (2014) using A-type stars suggests a sharp fall beyond 50 kpc. Finally, our modeling also enables us to place some limits on the anisotropy in the outer halo, and we find it to be $\beta = 0.4^{+0.2}_{-0.2}$.

Dark matter halo. We find that the mass of the dark matter halo is $0.80^{+0.31}_{-0.16} \times 10^{12} M_\odot$, and concentration is $21.1^{+14.8}_{-8.3}$. The upper uncertainty on concentration was found to be quite large. The mass estimate is lower and concentration estimate is higher than what has been previously measured. For a lower mass like ours, recent studies by Wang et al. (2012) and Vera-Ciro et al. (2013) suggest that the number of massive satellite galaxies, i.e., with $v_{max} > 30$ km s^{-1}, observed in the Galaxy matches predictions for ΛCDM halos of similar mass, potentially solving *the missing-satellite problem* at the high-mass end. We also

discussed other repercussions of the more concentrated and lighter Galaxy, e.g., all the classical satellite galaxies within the Galaxy were found to be bound.

Disk, bulge, and local parameters. Additional data in the inner region, i.e., the gas terminal velocity curve taken from Malhotra (1994, 1995) and the proper motion of the Sgr A* taken from Reid & Brunthaler (2004), also enable us to constrain the bulge and disk properties. The disk assumed to be of MN form has a mass of $0.95^{+0.24}_{-0.30} \times 10^{11} M_\odot$ and a scale length of $4.9^{+0.4}_{-0.4}$ kpc, while the bulge has a mass of $0.91^{+0.31}_{-0.38} \times 10^{10} M_\odot$.

Furthermore, it is important for a mass model of the Galaxy to agree with standard local constraints such as the escape velocity, the total column density integrated over $|z| \leqslant 1.1$ kpc, and the dark matter density. The escape velocity and the local dark matter density are in agreement with recent claims in the literature. Recent estimates of column density are slightly lower but within our quoted range. If the Sgr A* constraint is not used, our analysis independently suggests the angular velocity at the Sun to be $\omega_{LSR} = 30.2 \pm 1.2$ km s^{-1} kpc^{-1}.

In the end, we reiterate that our estimates of the mass parameters sensitively depend on the choices of $R_\odot$ and the outer power-law index of the tracer number density. The systematic uncertainties are of the order of (e.g., M_{vir}) and sometimes larger than (e.g., a) the random uncertainties. For example, we find that M_{vir} and c are directly proportional to the density slope. For each linear step of -0.5 from -4 to -5 we find that M_{vir} increases by $\sim30\%$ for each step, whereas c increases by $\sim20\%$ and M_{disk} and M_{bulge} decrease by $\sim22\%$ and $\sim20\%$, respectively. Further systematics inherent to the choices of parameters and assumptions we make in our anaylsis are discussed in detail in Section 5.9.

APPENDIX A

DIAGNOSTIC CRITERIA USED FOR SELECTING THE GIANT STARS

Out of 5330 candidate giant stars, the SSPP classifies 22 as K giant, 223 as red K giant, 3111 as *l*-color K giant, 536 as proper-motion K giant, and 1438 as M giant. For reference, the [Fe/H] distribution of 5330 stars is shown in Figure 11. The same distribution is used as a prior on metallicity while inferring the giant's distance.

To know how well the criteria listed in Equation (3) clean our catalog, we use code GALAXIA (Sharma et al. 2011a). GALAXIA has an analytical model based on Robin et al. (2003) and uses isochrones from the Padova database (Marigo et al. 2008; Bertelli et al. 1994) to compute photometric magnitudes for the model stars. First, we generate stars over an area of 8000 square degrees toward the north Galactic pole. For a fair comparison with observed data, the mock sample is then convolved with the typical errors in the photometric and stellar properties quoted by SDSS/SEGUE. According to the provided
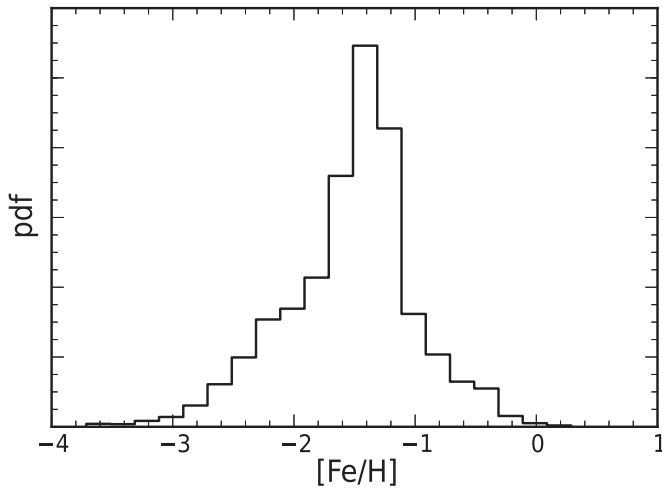
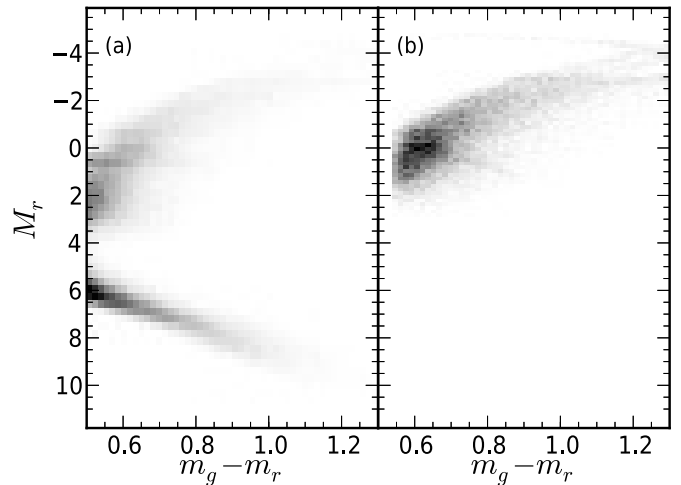**Figure 11.** Metallicity ([Fe/H]) distribution of the catalog of giant stars.

Figure 12. Color–magnitude diagram of the GALAXIA data: (a) CMD of total sample; (b) CMD after selecting stars according to Equation (3).

specifications, the uncertainties in the SSPP stellar parameters, the effective temperature ($T_{\rm eff}$), the surface gravity ($\log g$), and the metallicity ([Fe/H]), are 117 K, 0.26 dex, and 0.22 dex, respectively, which in reality also depend on the type and the signal-to-noise ratio of the spectra. Here we do not deal with the spectra and thus just assign gaussian random error to the stellar parameters and the metallicity with dispersion chosen to be the same as the above uncertainty values. We also convolve the mock data with the error in magnitude given by $\Delta m = 0.015 + 10^{-3+0.4(m-22.6)}$. This relation roughly matches to the errors in SDSS photometry (Jurić et al. 2008, Figure 7 with a systematic of 0.015).

The above "ideal" data once convolved with the observational errors are shown in a color–magnitude diagram (CMD) in Figure 12(a). Figure 12(b) is again the CMD for the mock data, but after imposing the set of cuts given in Equation (3) that we apply to obtain SEGUE giants. The final sample of stars remaining in our mock catalog is found to contain a negligible amount ($<0.5\%$) of dwarf contamination. This assures that our selection criteria perform well, at least for the theoretical data.

APPENDIX B

DISTANCE ESTIMATION

The procedure for distance estimation is the same as in Xue et al. (2014) but was implemented independently. We rely on the Bayes rule. It allows us to update an initial probability (prior) into a revised probability (posterior) and is written for our case as

$$p(\mu|S) \propto p(S|\mu) \times p(\mu). \tag{B1}$$

Here $\mu =$ apparent magnitude (m) $-$ absolute magnitude (M) is a distance modulus, whereas S represents a set of observables given by $S = \{m, c, [\mathrm{Fe/H}]\}$. The color c is assumed to be a function of M and [Fe/H]. In Equation (B1), the posterior $p(\mu|S)$ is the probability distribution of μ given the data S; the prior $p(\mu)$ is the information about μ known a priori; and the likelihood function $p(S|\mu)$ gives the likelihood of obtaining the data S given the μ. Here the likelihood function can be more explicitly written as

$$p(S|\mu) = \int\int \mathcal{P}(S|\mu)\, p(M)\, p([\mathrm{Fe/H}])\, dM\, d[\mathrm{Fe/H}], \tag{B2}$$

where the functional form for the probability $\mathcal{P}(S|\mu)$ is given by

$$\begin{aligned}\mathcal{P}(S|\mu) = \mathcal{P}(m, c, [\mathrm{Fe/H}]|\mu) &= \mathcal{N}(c|c', \sigma_c)\\ &\times \mathcal{N}(\mu + M|m', \sigma_m) \times \mathcal{N}([\mathrm{Fe/H}]|[\mathrm{Fe/H}]', \sigma_{[\mathrm{Fe/H}]}).\end{aligned} \tag{B3}$$

Here m', c', [Fe/H]$'$ are the observables for each star and σ_m, σ_c, $\sigma_{[\mathrm{Fe/H}]}$ are the associated uncertainties, respectively. In Equation (B2), the probability function $\mathcal{P}(S|\mu)$ is weighed with the luminosity $p(M)$ and metallicity $p([\mathrm{Fe/H}])$ prior probabilities. The theoretical (Salaris et al. 2002) and observational evidence (Langer et al. 2000) suggests that the luminosity function of the giants follows a power law. Therefore, fitting a power law to the luminosity function of the red giant branch (RGB) stars in the globular clusters, namely, M5 and M30, shown in the Figures 2 (for M5) and 4 (for M30) of Langer et al. (2000), we determine a common slope of 0.32. This leads to the final expression for a prior on the luminosity function given by $p(M) = 10^{0.32M}/17.79$, which is normalized to unity in the data range $M \in [-3.5, 3.5]$. The magnitude of the RGB star has been found to be independent of the metallicity content (Salaris et al. 2002), and hence we neglect the effect of the stellar metal content in our luminosity priors. A prior for the metallicity $p([\mathrm{Fe/H}])$ is chosen to be the same as the [Fe/H] distribution of the data, shown in Figure 11. The color c is a function of magnitude m and metallicity [Fe/H]. Hence, we do not need to explicitly assume a prior for the color, but a relation between c, m, and [Fe/H] has to be defined. We derive this relation from the available isochrones of three globular clusters, namely, M92, M13, and M71, and an open cluster NGC 6791 taken from An et al. (2008, and references therein). The [Fe/H] values for M92, M13, and M71 are taken to be -2.38, -1.60, and -0.81 (Kraft & Ivans 2003; An et al. 2008), respectively, whereas for NGC 6791 it is assumed to be +0.40 (An et al. 2008). The distance moduli are taken to be 14.64 for M92, 14.38 for M13 (Carretta et al. 2000), 12.86 for M71 (Grundahl et al. 2002), and 13.02 for NGC 6791 (Harris 1996). The color–magnitude–metallicity relation hence obtained is similar to Figure 2 of Karaali et al. (2013) and Figure 5 of Xue et al. (2014). The obtained fiducials (color–magnitude curves) are found to be well approximated by the seventh-order polynomial fit. The coefficients of the polynomial are then linearly interpolated in order to fill the gaps between the available isochrones
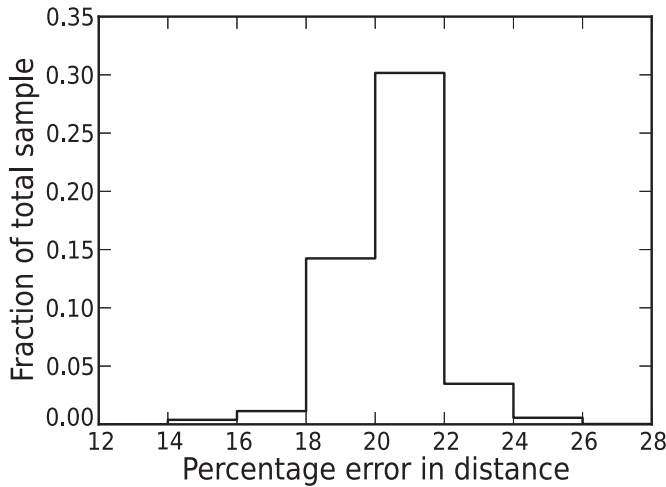
Figure 13. Percentage errors in distance estimation of K-giant catalog.

RA (deg)	Dec (deg)	m_r	$m_g - m_r$	[Fe/H]	d (kpc)
356.3899	13.8537	17.72 ± 0.01	0.61 ± 0.02	-1.34 ± 0.04	16.0 ± 2.8
358.2260	36.1001	17.72 ± 0.01	0.91 ± 0.02	-2.78 ± 0.01	49.8 ± 9.0
53.4036	0.0291	16.07 ± 0.01	0.69 ± 0.02	-1.06 ± 0.06	21.6 ± 5.0
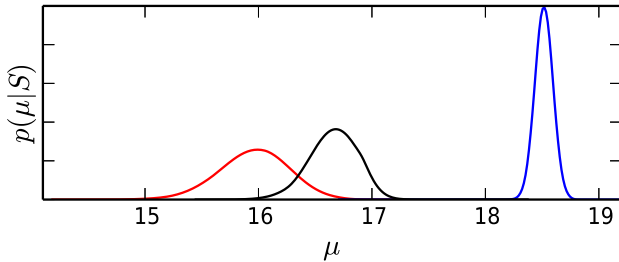
Figure 14. Likelihood distributions of the distance moduli of three giant stars and the effect of priors. The red, black, and blue lines display the posteriors of the distance probabilities $p(\mu|S)$ for three different stars with coordinates Right Ascension (RA) and declination (Dec) given in the J2000 epoch; magnitude r; color $g-r$; metallicity [Fe/H] in dex; and distance d in kiloparsecs shown in colored texts above the plots.

(A color version of this figure is available in the online journal.)

of the clusters. Given a color $g - r$ and [Fe/H] for a star, the interpolated fiducial sequences are then used to compute the corresponding value of the magnitude M_r.

Finally, to compute the posterior distribution $p(\mu|S)$ for an individual star (Equation (B1)), we also need to consider a distance prior $p(\mu)$. Recent observational evidence (e.g., Watkins et al. 2009; Deason et al. 2011; Akhter et al. 2012, etc) supports a broken power law for the density distribution of the halo stars. As a convenient summary of all these works, we assume $\rho \propto r^{-\alpha}$, with an inner slope of 2.4, an outer slope of 4.5, and a break at radius 25 kpc. The change of variables is done using $p(\mu)d\mu = p(r)dr = 4\pi r^2 \rho(r)dr$. Using the photometric parallax relation $d/\mathrm{kpc} = 10^{(\mu/5-2)}$ and assuming that $d \approx r$, our final expression for the distance prior is $p(\mu) = (4/5)\pi \ln(10)r^3 \rho(r)$. The uncertainties in the distance measurement of our catalog are shown in Figure 13. This is computed from the 16th and 84th percentiles of $p(\mu|S)$ of stars.

As an example of this approach, in Figure 14 we present results for three arbitrary giants from our catalog. The colored texts at the top of the figure provide the position in right ascension (RA) and declination (Dec), magnitude m_r, color $m_g - m_r$,

metallicity [Fe/H], and distance d for the corresponding stars shown in the same color on the immediate figures underneath, which show the posteriors of distance probabilities $p(\mu|S)$.

REFERENCES

Abadi, M. G., Navarro, J. F., & Steinmetz, M. 2006, MNRAS, 365, 747
Ahn, C. P., Alexandroff, R., Allende Prieto, C., et al. 2012, ApJS, 203, 21
Akhter, S., Da Costa, G. S., Keller, S. C., & Schmidt, B. P. 2012, ApJ, 756, 23
An, D., Johnson, J. A., Clem, J. L., et al. 2008, ApJS, 179, 326
Bahcall, J. N., & Tremaine, S. 1981, ApJ, 244, 805
Battaglia, G., Helmi, A., Morrison, H., et al. 2005, MNRAS, 364, 433
Bell, E. F., Zucker, D. B., Belokurov, V., et al. 2008, ApJ, 680, 295
Bertelli, G., Bressan, A., Chiosi, C., Fagotto, F., & Nasi, E. 1994, A&AS, 106, 275
Bhattacharjee, P., Chaudhury, S., & Kundu, S. 2014, ApJ, 785, 63
Binney, J. 2013, NewAR, 57, 29
Binney, J., & Merrifield, M. (ed.) 1998, Galactic Astronomy (Princeton, NJ: Princeton Univ. Press)
Binney, J., & Tremaine, S. 2008, Galactic Dynamics (2nd ed.; Princeton, NJ: Princeton Univ. Press)
Bissantz, N., & Gerhard, O. 2002, MNRAS, 330, 591
Bond, N. A., Ivezić, Ž., Sesar, B., et al. 2010, ApJ, 716, 1
Bovy, J., & Rix, H.-W. 2013, ApJ, 779, 115
Bovy, J., Rix, H.-W., Liu, C., et al. 2012, ApJ, 753, 148
Bovy, J., & Tremaine, S. 2012, ApJ, 756, 89
Boylan-Kolchin, M., Bullock, J. S., & Kaplinghat, M. 2011, MNRAS, 415, L40
Boylan-Kolchin, M., Bullock, J. S., Sohn, S. T., Besla, G., & van der Marel, R. P. 2013, ApJ, 768, 140
Brown, W. R., Geller, M. J., Kenyon, S. J., & Diaferio, A. 2010, AJ, 139, 59
Bryan, G. L., & Norman, M. L. 1998, ApJ, 495, 80
Bullock, J. S. 2010, arXiv:1009.4505
Bullock, J. S., & Johnston, K. V. 2005, ApJ, 635, 931
Bullock, J. S., Kolatt, T. S., Sigad, Y., et al. 2001, MNRAS, 321, 559
Carignan, C., & Freeman, K. C. 1985, ApJ, 294, 494
Carlin, J. L., Majewski, S. R., Casetti-Dinescu, D. I., et al. 2012, ApJ, 744, 25
Carretta, E., Gratton, R. G., Clementini, G., & Fusi Pecci, F. 2000, ApJ, 533, 215
Catena, R., & Ullio, P. 2010, JCAP, 08, 004
Courteau, S., Cappellari, M., de Jong, R. S., et al. 2014, RvMP, 86, 47
Deason, A. J., Belokurov, V., & Evans, N. W. 2011, MNRAS, 416, 2903
Deason, A. J., Belokurov, V., Evans, N. W., et al. 2012, MNRAS, 425, 2840
Deason, A. J., Belokurov, V., Koposov, S. E., & Rockosi, C. M. 2014, ApJ, 787, 30
Deason, A. J., Van der Marel, R. P., Guhathakurta, P., Sohn, S. T., & Brown, T. M. 2013, ApJ, 766, 24
Dehnen, W., & Binney, J. 1998, MNRAS, 294, 429
Dehnen, W., McLaughlin, D. E., & Sachania, J. 2006, MNRAS, 369, 1688
Duffy, A. R., Schaye, J., Kay, S. T., & Dalla Vecchia, C. 2008, MNRAS, 390, L64
Francis, C., & Anderson, E. 2014, MNRAS, 441, 1105
Gillessen, S., Eisenhauer, F., Fritz, T. K., et al. 2013, in IAU Symp. 289, Advancing the Physics of Cosmic Distances, ed. R. de Grijs (Cambridge: Cambridge Univ. Press), 29
Gilmore, G., & Reid, N. 1983, MNRAS, 202, 1025
Goodman, J., & Weare, J. 2010, CMaPh, 5, 65
Grundahl, F., Stetson, P. B., & Andersen, M. I. 2002, A&A, 395, 481
Harris, W. E. 1996, AJ, 112, 1487
Hattori, K., Yoshii, Y., Beers, T. C., Carollo, D., & Lee, Y. S. 2013, ApJL, 763, L17
Holmberg, J., & Flynn, C. 2000, MNRAS, 313, 209
Holmberg, J., & Flynn, C. 2004, MNRAS, 352, 440
Hunter, J. D. 2007, CSE, 9, 90
Irrgang, A., Wilcox, B., Tucker, E., & Schiefelbein, L. 2013, A&A, 549, A137
Jeans, J. H. 1915, MNRAS, 76, 70
Johnston, K. V. 1998, ApJ, 495, 297
Jurić, M., Ivezić, Ž., Brooks, A., et al. 2008, ApJ, 673, 864
Kafle, P. R., Sharma, S., Lewis, G. F., & Bland-Hawthorn, J. 2012, ApJ, 761, 98
Kafle, P. R., Sharma, S., Lewis, G. F., & Bland-Hawthorn, J. 2013, MNRAS, 430, 2973
Kahn, F. D., & Woltjer, L. 1959, ApJ, 130, 705
Kallivayalil, N., van der Marel, R. P., Besla, G., Anderson, J., & Alcock, C. 2013, ApJ, 764, 161
Karaali, S., Bilir, S., & Gökçe, E. Y. 2013, PASA, 30, 8

Kauffmann, G., White, S. D. M., & Guiderdoni, B. 1993, MNRAS, 264, 201
King, L. J., & Mead, J. M. G. 2011, MNRAS, 416, 2539
Klypin, A., Kravtsov, A. V., Valenzuela, O., & Prada, F. 1999, ApJ, 522, 82
Komatsu, E., Smith, K. M., Dunkley, J., et al. 2011, ApJS, 192, 18
Kraft, R. P., & Ivans, I. I. 2003, PASP, 115, 143
Kregel, M., van der Kruit, P. C., & Freeman, K. C. 2005, MNRAS, 358, 503
Kuijken, K., & Gilmore, G. 1989a, MNRAS, 239, 605
Kuijken, K., & Gilmore, G. 1989b, MNRAS, 239, 651
Kuijken, K., & Gilmore, G. 1989c, MNRAS, 239, 571
Kuijken, K., & Gilmore, G. 1991, ApJL, 367, L9
Langer, G. E., Bolte, M., & Sandquist, E. 2000, ApJ, 529, 936
Law, D. R., Johnston, K. V., & Majewski, S. R. 2005, ApJ, 619, 807
Law, D. R., & Majewski, S. R. 2010, ApJ, 714, 229
Leonard, P. J. T., & Tremaine, S. 1990, ApJ, 353, 486
Li, Y.-S., & White, S. D. M. 2008, MNRAS, 384, 1459
Lin, D. N. C., & Lynden-Bell, D. 1982, MNRAS, 198, 707
Macciò, A. V., Dutton, A. A., van den Bosch, F. C., et al. 2007, MNRAS, 378, 55
Malhotra, S. 1994, ApJ, 433, 687
Malhotra, S. 1995, ApJ, 448, 138
Marigo, P., Girardi, L., Bressan, A., et al. 2008, A&A, 482, 883
McClure-Griffiths, N. M., & Dickey, J. M. 2007, ApJ, 671, 427
McMillan, P. J. 2011, MNRAS, 414, 2446
McMillan, P. J., & Binney, J. J. 2010, MNRAS, 402, 934
Méndez, R. A., Platais, I., Girard, T. M., Kozhurina-Platais, V., & van Altena, W. F. 1999, ApJL, 524, L39
Miyamoto, M., & Nagai, R. 1975, PASJ, 27, 533
Moore, B., Ghigna, S., Governato, F., et al. 1999, ApJL, 524, L19
Morrison, H. L., Flynn, C., & Freeman, K. C. 1990, AJ, 100, 1191
Navarro, J. F., Frenk, C. S., & White, S. D. M. 1996, ApJ, 462, 563
Newberg, H. J., Willett, B. A., Yanny, B., & Xu, Y. 2010, ApJ, 711, 32
Nichols, M., Revaz, Y., & Jablonka, P. 2014, MNRAS, 442, 2883
Nikiforov, I. 2004, in ASP Conf. Ser. 316, Order and Chaos in Stellar and Planetary Systems, ed. G. G. Byrd, K. V. Kholshevnikov, A. A. Myllri, I. I. Nikiforov, & V. V. Orlov (San Francisco, CA: ASP), 199
Olling, R. P., & Merrifield, M. R. 1998, MNRAS, 297, 943
Oort, J. H. 1932, BAN, 6, 249
Pawlowski, M. S., & Kroupa, P. 2013, MNRAS, 435, 2116
Pérez, F., & Granger, B. E. 2007, CSE, 9, 21
Piffl, T., Scannapieco, C., Binney, J., et al. 2014, A&A, 562, A91
Planck Collaboration, Ade, P. A. R., Aghanim, N., et al. 2013, arXiv:1303.5076
Ratnatunga, K. U., Bahcall, J. N., & Casertano, S. 1989, ApJ, 339, 106
Ratnatunga, K. U., & Freeman, K. C. 1989, ApJ, 339, 126
Reid, M. J. 1993, ARA&A, 31, 345
Reid, M. J., & Brunthaler, A. 2004, ApJ, 616, 872
Reid, M. J., Menten, K. M., Brunthaler, A., et al. 2014, ApJ, 783, 130
Robin, A. C., Reylé, C., Derrière, S., & Picaud, S. 2003, A&A, 409, 523

Robotham, A. S. G., Baldry, I. K., Bland-Hawthorn, J., et al. 2012, MNRAS, 424, 1448
Sackett, P. D. 1997, ApJ, 483, 103
Salaris, M., Cassisi, S., & Weiss, A. 2002, PASP, 114, 375
Sales, L. V., Navarro, J. F., Abadi, M. G., & Steinmetz, M. 2007, MNRAS, 379, 1464
Sanders, J. L., & Binney, J. 2013a, MNRAS, 433, 1813
Sanders, J. L., & Binney, J. 2013b, MNRAS, 433, 1826
Sanderson, R. E., & Helmi, A. 2013, MNRAS, 435, 378
Schlegel, D. J., Finkbeiner, D. P., & Davis, M. 1998, ApJ, 500, 525
Schönrich, R., Binney, J., & Asplund, M. 2012, MNRAS, 420, 1281
Schönrich, R., Binney, J., & Dehnen, W. 2010, MNRAS, 403, 1829
Sesar, B., Ivezić, Ž., Lupton, R. H., et al. 2007, AJ, 134, 2236
Sesar, B., Ivezić, Ž., Stuart, J. S., et al. 2013, AJ, 146, 21
Sesar, B., Jurić, M., & Ivezić, Ž. 2011, ApJ, 731, 4
Sharma, S., Bland-Hawthorn, J., Johnston, K. V., & Binney, J. 2011a, ApJ, 730, 3
Sharma, S., Johnston, K. V., Majewski, S. R., Bullock, J., & Muñoz, R. R. 2011b, ApJ, 728, 106
Sharma, S., Steinmetz, M., & Bland-Hawthorn, J. 2012, ApJ, 750, 107
Sirko, E., Goodman, J., Knapp, G. R., et al. 2004, AJ, 127, 899
Smith, M. C., Evans, N. W., Belokurov, V., et al. 2009a, MNRAS, 399, 1223
Smith, M. C., Ruchti, G. R., Helmi, A., et al. 2007, MNRAS, 379, 755
Smith, M. C., Wyn Evans, N., & An, J. H. 2009b, ApJ, 698, 1110
Sofue, Y. 2013, in Planets, Stars, and Stellar Systems, Vol. 5: Galactic Structure and Stellar Populations, ed. T. D. Oswalt & G. Gilmore (Berlin: Springer), 985
Sofue, Y., Honma, M., & Omodaka, T. 2009, PASJ, 61, 227
Springel, V., Wang, J., Vogelsberger, M., et al. 2008, MNRAS, 391, 1685
Strigari, L. E. 2013, PhR, 531, 1
van Albada, T. S., Bahcall, J. N., Begeman, K., & Sancisi, R. 1985, ApJ, 295, 305
Vera-Ciro, C. A., Helmi, A., Starkenburg, E., & Breddels, M. A. 2013, MNRAS, 428, 1696
Wang, J., Frenk, C. S., Navarro, J. F., Gao, L., & Sawala, T. 2012, MNRAS, 424, 2715
Watkins, L. L., Evans, N. W., & An, J. H. 2010, MNRAS, 406, 264
Watkins, L. L., Evans, N. W., Belokurov, V., et al. 2009, MNRAS, 398, 1757
Wechsler, R. H., Bullock, J. S., Primack, J. R., Kravtsov, A. V., & Dekel, A. 2002, ApJ, 568, 52
Widrow, L. M., Pym, B., & Dubinski, J. 2008, ApJ, 679, 1239
Xue, X.-X., Ma, Z., Rix, H.-W., et al. 2014, ApJ, 784, 170
Xue, X.-X., Rix, H.-W., Yanny, B., et al. 2011, ApJ, 738, 79
Xue, X. X., Rix, H. W., Zhao, G., et al. 2008, ApJ, 684, 1143
Yanny, B., Newberg, H. J., Kent, S., et al. 2000, ApJ, 540, 825
Yanny, B., Rockosi, C., Newberg, H. J., et al. 2009, AJ, 137, 4377
Zhang, L., Rix, H.-W., van de Ven, G., et al. 2013, ApJ, 772, 108